Robotica (2026), **44**, pp. 1743–1765
doi:10.1017/S0263574726103774

CAMBRIDGE UNIVERSITY PRESS

RESEARCH ARTICLE

Performance analysis and optimization of a modified Schoenflies motion parallel manipulator with decoupled pitch motion

Xiaoshu Zhang[1], Aihong Ji[1,2], Shikun Wen[1], Andong Jiang[1], Yi Sun[1], Zhikang Yang[1] and Qian Qi[1]

[1]Lab of Locomotion Bioinspiration and Intelligent Robots, College of Mechanical and Electrical Engineering, Nanjing University of Aeronautics and Astronautics, Nanjing, China
[2]State Key Laboratory of Mechanics and Control for Aerospace Structures, Nanjing University of Aeronautics and Astronautics, Nanjing, China
Corresponding author: Aihong Ji; Email: meeahji@nuaa.edu.cn

Received: 29 December 2025 UTC; **Revised:** 23 May 2026 UTC; **Accepted:** 24 June 2026 UTC;
First published online: 29 July 2026 UTC

Keywords: parallel manipulator; 3T1R; kinematic analysis; stiffness analysis; multi-objective optimization

Abstract

The 4-DOF (four degrees of freedom)parallel manipulator, namely 2PPaRR-2PPaRU, offers three translations and one rotation capabilities, boasting an extensive rotation range, and a regular workspace. Moreover, its workspace can infinitely extend in conjunction with the extension of the driving joints. Nonetheless, the symmetric structure relying on Pa joint design presents performance challenges in the initial configuration and complicates the analytical solution of the forward kinematics, thereby increasing the complexity of dynamics and control. To address these limitations, the structure of the moving platform is modified by coaxially connecting the three joints at the ends of the three limbs to the moving platform. This improvement is followed by analyses of mobility, motion/force transmissibility, and stiffness. The overall reachable workspace area, good transmission workspace ratio, and global stiffness index are then chosen as key objectives for dimensional optimization, thereby achieving satisfactory performance for the new 3T1R PM. Finally, the CAD model with the selected parameters is presented, together with the distributions of motion/force transmission index and virtual stiffness index within the reachable workspace. The results validate the effectiveness of the optimization design.

1. Introduction

The Schoenflies motion represents the end effector of a parallel manipulator (PM) with 3-DOF for translation and 1-DOF for rotation around a fixed axis [1]. This type of manipulator finds wide applications in various industries, including packing, pick and place, and painting [2]. Over the past decades, numerous 3T1R (3-translation and 1-rotation) PMs have been discussed in the literature [3–7]. Topology characteristic-based methods [8], constraint screw theory [9], and Lie group theory [10] have been extensively applied in the type synthesis of 3T1R PMs. Depending on the rotation mode of the moving platform (MP), 3T1R PMs can be classified into the articulated MP type [5–7], the helical joint connected MP type [11], and the single MP type [12]. Among these types, the 3T1R PM with a single MP stands out due to its simple structure and lightweight moving parts. However, most single MP 3T1R PMs have relatively limited regular workspaces when subjected to certain actuated joint stroke limitations, which restricts their applicability.

To address this limitation, we have proposed a 3T1R PM with the 2PPaRR-2PPaRU configuration in Ref. [12]. Compared with the existing 3T1R PM 2PRPaR-2PRPaU [13], the sequence of parallelogram (Pa) joints and revolute (R) joints in all four limbs is changed from R-Pa to Pa-R. This modification reduces the influence of driving joint stroke on the cross-sectional profile of the reachable workspace, thus resulting in a more regular workspace. However, symmetric 3T1R PMs based on Pa joints typically

© The Author(s), 2026. Published by Cambridge University Press.

Downloaded from https://www.cambridge.org/core. UNIVERSIDAD AUTONOMA METROPOLITANA, on 16 Nov 2026 at 18:24:25, subject to the Cambridge Core terms of use, available at https://www.cambridge.org/core/terms. https://doi.org/10.1017/S0263574726103774

exhibit poor performance in their home configurations and often encounter architectural singularities, which limits their practical use. Two primary approaches exist to address architectural singularities in such PMs: adjusting the mechanism's structural parameters [14–18] or employing redundant actuation [19]. While redundant actuation increases the complexity and control challenges, most current solutions rely on adjusting structural parameters. For instance, Angeles et al. [14, 15] examined the influence of the shape and size of the Stewart PM's MP on singularity and performance. Lou et al. [16] mitigated the architectural singularity of the mechanism at its initial configuration by aligning the end revolute joints of the 2nd, 3rd, and 4th limbs. Kim et al. [17] eliminated the architectural singularity in the initial configuration by rearranging the limbs on the MP, while Salgado et al. [18] positioned the limbs on an asymmetric frame to avoid architectural singularity. However, most of these methods do not achieve rotational decoupling [14, 15, 17, 18]. Based on the method in Ref. [16], we present an improved 3T1R PM, termed 2PPaRR-2PPaRU, which features an analytical solution for forward kinematics. This enhanced 3T1R PM retains the benefits of the original mechanism, such as a regular workspace and a large rotational range. Moreover, it overcomes the architectural singularity at the initial configuration and achieves rotational decoupling, thereby simplifying kinematic analysis and enhancing mechanism control.

Performance analysis is crucial for evaluating the performance and optimizing parameters of PMs. Kinematic performance evaluation mainly includes dexterity [20], manipulability [21], and motion/force transmission index [22, 23]. Compared with the Jacobian-based indexes [20, 21], the motion/force transmission index [22, 23] reflects the efficiency of energy transfer from inputs to outputs, a vital indicator of the manipulator's operational performance. To ensure the optimized parameters meet the accuracy requirements in application scenes, such as seeding transplanting, pipe cultivation, packing etc., the stiffness model of the modified 3T1R PM is established through the virtual joint method (VJM) [24–27]. The VSI [28] is applied to evaluate the stiffness performance.

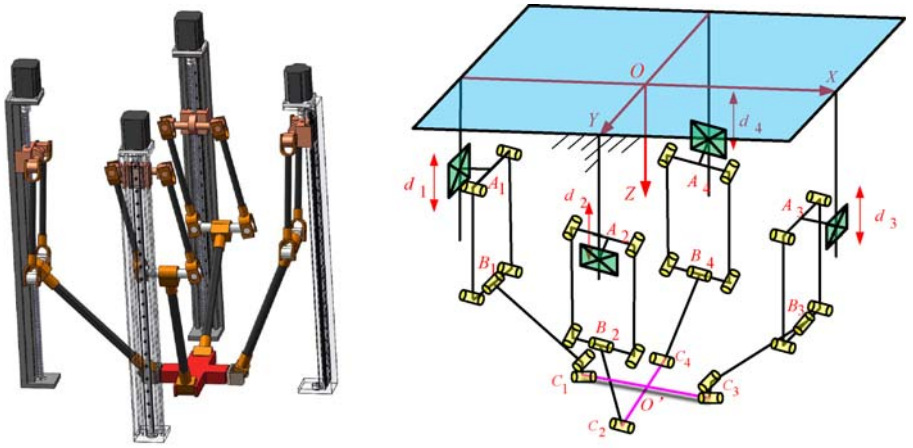
The remainder of this paper is organized as follows: Section 2 introduces the modified 3T1R PM structure and presents the mobility analysis. In Section 3, the authors derive analytical solutions for the forward and inverse kinematics of the manipulator. Section 4 conducts a singularity analysis based on the Jacobian matrix of the mechanism. The motion/force transmission index is analyzed in Section 5. The stiffness model of the modified PM is established, and its stiffness performance is evaluated in Section 6. Section 7 presents parameter optimization based on the overall reachable workspace area (ORWA), the good transmission workspace (GTW) ratio (GTWR), and global stiffness index (GSI). Finally, Section 8 summarizes the paper.

2. Structure and mobility analysis

The original structure of the 4-DOF 3T1R PM 2PPaRR-2PPaRU [12] is depicted in Figure 1. In this configuration, the two PPaRU limbs (the 1st and 3rd limbs) and the two PPaRR limbs (the 2nd and 4th limbs) are symmetrically arranged on the base. The axes of the four prismatic (P) joints align with the $\boldsymbol{Z}$-axis, while the movement direction of the Pa joints lies in the plane of the Pa joints and is perpendicular to the link $A_iB_i(i = 1, 2, 3, 4)$. The axes of the revolute joints in limbs 2 and 4 run parallel to the $\boldsymbol{Y}$-axis. Additionally, the axes of the revolute joints and the first revolute joints of the universal joints in limbs 1 and 3 are parallel to the $\boldsymbol{X}$-axis, while the axes of the second revolute joints of the universal joints are parallel to the $\boldsymbol{Y}$-axis. There are three translations at the end of the four limbs, one rotation around the $\boldsymbol{Y}$-axis at the end of limbs 2 and 4, and two rotational motions with axes parallel to the $\boldsymbol{X}$ and $\boldsymbol{Y}$ axes at the end of limbs 1 and 3.

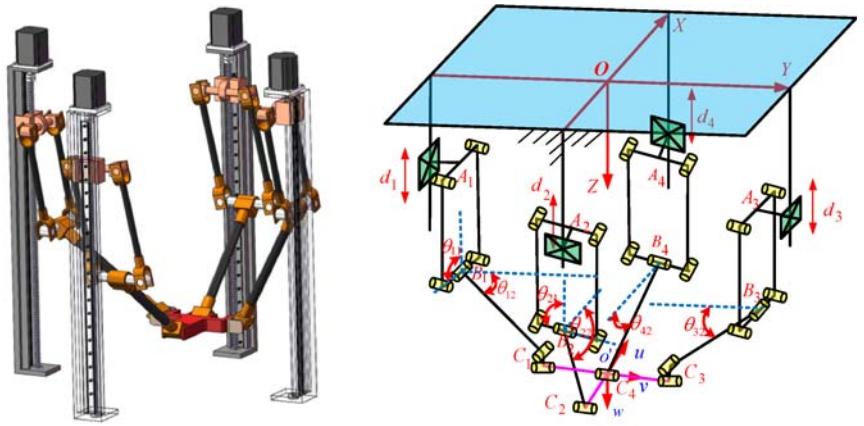
Utilizing the constraint screw theory [29], it is possible to determine the mobility and motion characteristics of the MP. However, the symmetric design based on Pa joints often leads to poor performance or even architectural singularity of the 3T1R PM at its home configuration. Additionally, the rotation of the MP is strongly coupled with limbs 2 and 4, increasing the complexity of kinematic analysis and control for the mechanism.

Downloaded from https://www.cambridge.org/core. UNIVERSIDAD AUTONOMA METROPOLITANA, on 16 Nov 2026 at 18:24:25, subject to the Cambridge Core terms of use, available at https://www.cambridge.org/core/terms. https://doi.org/10.1017/S0263574726103774



(a) **(b)**

Figure 1. *The original 2PPaRR-2PPaRU PM. (a) CAD model and (b) schematic representation.*



(a) **(b)**

Figure 2. *The improved 3T1R PM 2PPaRR-2PPaRU. (a) CAD model and (b) schematic representation.*

To address these issues, the authors have coaxially connected the end revolute joints of limbs 1, 3, and 4 to the MP. The geometric center of the revolute joint C_4 in limb 4 has been selected as the origin o' of the moving coordinate system. Figure 2(a) presents a three-dimensional (3D) model of the improved 3T1R PM, while Figure 2(b) provides a schematic representation of the mechanism. Table I lists the structural parameters of the improved 2PPaRR-2PPaRU PM.

The constraint screw theory [29] is employed to analyze the mobility of the enhanced 2PPaRR-2PPaRU PM. The twist screw systems of limbs 1 and 2 can be expressed as follows:

$$\begin{cases} \$_{11} = (\mathbf{0}; \boldsymbol{z}) \,, \$_{12} = \left(\mathbf{0}; \boldsymbol{u}_{a_1 b_1} \times \boldsymbol{y}\right) \\ \$_{13} = (\boldsymbol{x}; \boldsymbol{r}_{B1} \times \boldsymbol{x}) \,, \$_{14} = (\boldsymbol{x}; \boldsymbol{r}_{C1} \times \boldsymbol{x}) \\ \$_{15} = (\boldsymbol{y}; \boldsymbol{r}_{C1} \times \boldsymbol{y}) \end{cases} \tag{1}$$

and

$$\begin{cases} \$_{21} = (\mathbf{0}; \boldsymbol{z}) \,, \$_{22} = \left(\mathbf{0}; \boldsymbol{u}_{a_2 b_2} \times \boldsymbol{x}\right) \\ \$_{23} = (\boldsymbol{y}; \boldsymbol{r}_{B2} \times \boldsymbol{y}) \,, \$_{24} = (\boldsymbol{y}; \boldsymbol{r}_{C2} \times \boldsymbol{y}) \end{cases} \tag{2}$$

Downloaded from https://www.cambridge.org/core. UNIVERSIDAD AUTONOMA METROPOLITANA, on 16 Nov 2026 at 18:24:25, subject to the Cambridge Core terms of use, available at https://www.cambridge.org/core/terms. https://doi.org/10.1017/S0263574726103774

Table I. *The structure parameters of the improved 2PPaRR-2PPaRU PM*

Symbol	Description	Unit
a_1	The half distance between A_1 and A_3	mm
a_2	The half distance between A_2 and A_4	mm
l_1	The distance between segment $A_iB_i(i=1,2,3,4)$	mm
l_2	The distance between segment $B_iC_i(i=1,2,3,4)$	mm
b_1	The distance between C_2 and C_4	mm
b_2	The half distance between C_1 and C_3	mm

where $\boldsymbol{x}$, $\boldsymbol{y}$ and $\boldsymbol{z}$ denote the unit direction vectors of the $\boldsymbol{X}$, $\boldsymbol{Y}$ and $\boldsymbol{Z}$ axes, respectively; $\boldsymbol{r}_{Bi}$ and $\boldsymbol{r}_{Ci}(i=1,2)$ denote the geometric centers of the joints, and $\boldsymbol{u}_{a_ib_i}$ and $\boldsymbol{u}_{b_ic_i}(i=1,2)$ represent the unit directional vectors of links A_iB_i and $B_iC_i(i=1,2)$. Based on the reciprocal relationship between the twist screw system and the wrench screw system, the constraint screw applied by limbs 1 and 2 can be determined as follows:

$$\$_{C11} = (0,0,0;0,0,1) \tag{3}$$

and

$$\begin{cases} \$_{C21} = (0,0,0;0,0,1) \\ \$_{C22} = (0,0,0;1,0,0) \end{cases} \tag{4}$$

where the $\$_{Cij}$ expresses the constraint wrench screw exerted on the MP by the limb i. Similarly, the constraint wrench screw systems of the limbs 3 and 4 can be written as:

$$\$_{C31} = (0,0,0;0,0,1) \tag{5}$$

and

$$\begin{cases} \$_{C41} = (0,0,0;0,0,1) \\ \$_{C42} = (0,0,0;1,0,0) \end{cases} \tag{6}$$

Note that $\$_{C11} = \$_{C21} = \$_{C31} = \$_{C41}$ and $\$_{C22} = \$_{C42}$, which means the 3T1R PM 2PPaRR-2PPaRU is an over-constrained system. The constraint wrench screw system of the 3T1R PM 2PPaRR-2PPaRU can be derived through Eqs. (3)–(6) as:

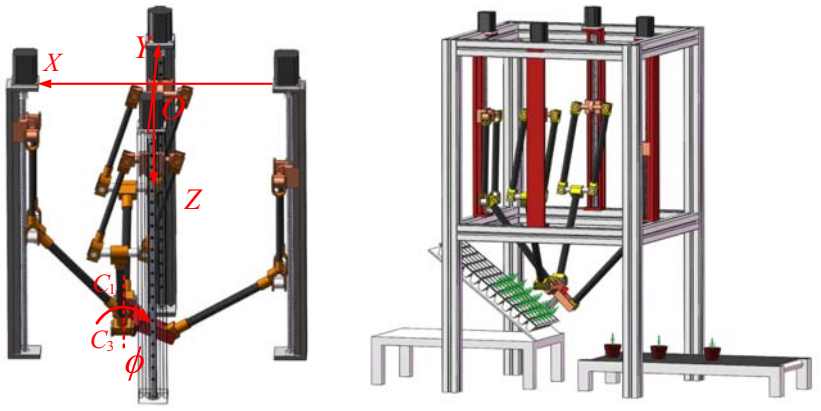
$$\begin{cases} \$_{C1} = (0,0,0;1,0,0) \\ \$_{C2} = (0,0,0;0,0,1) \end{cases} \tag{7}$$

Reusing the reciprocal screw theory, the twist screw system of the mechanism can be derived as:

$$\begin{cases} \$_1 = (0,0,0;1,0,0) \\ \$_2 = (0,0,0;0,1,0) \\ \$_3 = (0,0,0;0,0,1) \\ \$_4 = (0,1,0;0,0,0) \end{cases} \tag{8}$$

Eq. (8) indicates that the 2PPaRR-2PPaRU PM offers three translations and one rotation around the $\boldsymbol{Y}$-axis. Figure 3(a) illustrates the MP after undergoing finite rotation about the $\boldsymbol{Y}$-axis, while Figure 3(b) demonstrates the application of the 2PPaRR-2PPaRU PM in transplanting seedlings. When the 4-DOF PM performs seedling transplanting, the MP is parallel to the seedling tray, and the gripper on the MP grips the seedling; then the MP moves with the seedling. Subsequently, the orientation of the MP gradually becomes parallel to the transmission belt ($\phi = 0$). Once the MP reaches the fixed transplanting position, the gripper puts the seedling into the flowerpot. Compared with the 1-DOF and the 2-DOF seedling transplanting mechanisms, the 4-DOF PM 2PPaRR-2PPaRU has better flexibility and can realize more trajectories.

Downloaded from https://www.cambridge.org/core. UNIVERSIDAD AUTONOMA METROPOLITANA, on 16 Nov 2026 at 18:24:25, subject to the Cambridge Core terms of use, available at https://www.cambridge.org/core/terms. https://doi.org/10.1017/S0263574726103774



(a) **(b)**

Figure 3. *Mobility and application of the improved 3T1R PM. (a) rotation around the Y-axis and (b) application.*

3. Position analysis

3.1. Inverse position analysis

Inverse position analysis aims to solve for the inputs of the driving joints d_i ($i = 1, 2, 3, 4$) under the given position and orientation of the MP (x, y, z, ϕ). Here, d_i represents the displacement of each actuated joint along the $\boldsymbol{Z}$-axis; ϕ is the rotation angle about the $\boldsymbol{Y}$-axis, where clockwise rotation is defined as negative and counterclockwise as positive. As seen in Figure 2, from the origin O of the global coordinate system to the geometric centers C_i of the revolute joints, the closed-loop equation of limb i can be written as follows:

$$\boldsymbol{OC}_i = \boldsymbol{OA}_i + \boldsymbol{A}_i\boldsymbol{B}_i + \boldsymbol{B}_i\boldsymbol{C}_i \tag{9}$$

Projecting Eq. (9) along global coordinate axes $\boldsymbol{X}$, $\boldsymbol{Y}$ and $\boldsymbol{Z}$, the algebraic equation can be expressed as follows:

$$\begin{cases} x = l_1 \cos\theta_{11} \\ y - b_2 = -a_1 + l_2 \cos\theta_{12} \\ z = d_1 + l_1 \sin\theta_{11} + l_2 \sin\theta_{12} \end{cases} \tag{10}$$

$$\begin{cases} x - b_1 \cos\phi = -a_2 + l_2 \cos\theta_{22} \\ y = l_1 \cos\theta_{21} \\ z + b_1 \sin\phi = d_2 + l_1 \sin\theta_{21} + l_2 \sin\theta_{22} \end{cases} \tag{11}$$

$$\begin{cases} x = l_1 \cos\theta_{31} \\ y + b_2 = a_1 - l_2 \cos\theta_{32} \\ z = d_3 + l_1 \sin\theta_{31} + l_2 \sin\theta_{32} \end{cases} \tag{12}$$

$$\begin{cases} x = a_2 - l_2 \cos\theta_{42} \\ y = l_1 \cos\theta_{41} \\ z = d_4 + l_1 \sin\theta_{41} + l_2 \sin\theta_{42} \end{cases} \tag{13}$$

where the intermediate variable θ_{i1} denotes the angle between link A_iB_i and the negative direction of the $\boldsymbol{X}-$ axis for limbs $i = 1, 3$, or the angle between link A_iB_i and the negative direction of the $\boldsymbol{Y}-$ axis for limbs $i = 2, 4$. Similarly, θ_{i2} is defined as the acute angle between link B_iC_i and the $\boldsymbol{Y}-$ axis for $i = 1, 3$, and as the acute angle between link B_iC_i and the $\boldsymbol{X}-$axis for $i = 2, 4$.

Downloaded from https://www.cambridge.org/core. UNIVERSIDAD AUTONOMA METROPOLITANA, on 16 Nov 2026 at 18:24:25, subject to the Cambridge Core terms of use, available at https://www.cambridge.org/core/terms. https://doi.org/10.1017/S0263574726103774

By solving Eqs. (10)–(13), the inverse position results are as follows:

$$\begin{cases} d_1 = z - l_1 \sin\theta_{11} - l_2 \sin\theta_{12} \\ d_2 = z + b_1 \sin\phi - l_1 \sin\theta_{21} - l_2 \sin\theta_{22} \\ d_3 = z - l_1 \sin\theta_{31} - l_2 \sin\theta_{32} \\ d_4 = z - l_1 \sin\theta_{41} - l_2 \sin\theta_{42} \end{cases} \tag{14}$$

where $\theta_{11} = a\cos\frac{x}{l_1}, \theta_{12} = a\cos\frac{y-b_2+a_1}{l_2}, \theta_{21} = a\cos\frac{y}{l_1}, \theta_{22} = a\cos\frac{a_2+x-b_1\cos\phi}{l_2}, \theta_{31} = a\cos\frac{x}{l_1}$, $\theta_{32} = a\cos\frac{a_1-y-b_2}{l_2}, \theta_{41} = a\cos\frac{y}{l_1}, \theta_{42} = a\cos\frac{a_2-x}{l_2}$.

3.2. Forward position analysis

In contrast to the inverse position analysis, forward position analysis involves solving for the position vector (x, y, z, ϕ) of the MP for the given inputs $d_i (i = 1, 2, 3, 4)$. The position vectors of joints B_i and C_i in the fixed coordinate system are expressed as follows:

$$\begin{cases} \boldsymbol{B}_1 = (l_1\cos\theta_{11}, -a_1, d_1 + l_1\sin\theta_{11}), \boldsymbol{C}_1 = (x, y - b_2, z) \\ \boldsymbol{B}_2 = (-a_2, l_1\cos\theta_{21}, d_2 + l_1\sin\theta_{21}), \boldsymbol{C}_2 = (x - b_1\cos\phi, y, z + b_1\sin\phi) \\ \boldsymbol{B}_3 = (l_1\cos\theta_{31}, a_1, d_3 + l_1\sin\theta_{31}), \boldsymbol{C}_3 = (x, y + b_2, z) \\ \boldsymbol{B}_4 = (a_2, l_1\cos\theta_{41}, d_4 + l_1\sin\theta_{41}), \boldsymbol{C}_4 = (x, y, z) \end{cases} \tag{15}$$

According to the geometric constraints of the mechanism:

$$|\boldsymbol{B}_i\boldsymbol{C}_i| = l_2 \ (i = 1, 2, 3, 4) \tag{16}$$

Combining Eqs. (15)–(16) leads to

$$\begin{cases} (x - l_1\cos\theta_{11})^2 + (y - b_2 + a_1)^2 + (z - d_1 - l_1\sin\theta_{11})^2 = l_2^2 \\ (x - b_1\cos\phi + a_2)^2 + (y - l_1\cos\theta_{21})^2 + (z + b_1\sin\phi - d_2 - l_1\sin\theta_{21})^2 = l_2^2 \\ (x - l_1\cos\theta_{31})^2 + (y + b_2 - a_1)^2 + (z - d_3 - l_1\sin\theta_{31})^2 = l_2^2 \\ (x - a_2)^2 + (y - l_1\cos\theta_{41})^2 + (z - d_4 - l_1\sin\theta_{41})^2 = l_2^2 \end{cases} \tag{17}$$

From Figure 2, we can obtain $\theta_{11} = \theta_{31}, \theta_{21} = \theta_{41}, x = l_1\cos\theta_{11}, y = l_1\cos\theta_{21}$; consequently, all the intermediate variables in Eq. (17) can be eliminated. Then the forward kinematic solutions can be derived as:

$$\begin{cases} x = \left(2a_2E_1 - \sqrt{4a_2^2E_2^2l_1^2 - E_1^2E_2^2 + E_2^4l_1^2}\right) / \left(4a_2^2 + E_2^2\right) \\ y = \left(d_1^2 - d_3^2 + 2M_4\left(d_3 - d_1\right)\right) / \left(4\left(b_2 - a_1\right)\right), z = M_4 + \sqrt{l_1^2 - x^2} \\ \phi = 2a\tan\left(\left(K_2 - \sqrt{K_2^2 - K_3^2 + K_1^2}\right) / \left(K_1 + K_3\right)\right) \end{cases} \tag{18}$$

The intermediate variables in the Eq. (18) are as follows: $M_1 = 4((d_3 - d_1)^2 + 4(b_2 - a_1)^2)$,

$$M_2 = 4\left(d_3 - d_1\right)\left(d_1^2 - d_3^2\right) - 16\left(b_2 - a_1\right)^2\left(d_3 + d_1\right), M_4 = \left(-M_2 + \sqrt{M_2^2 - 4M_1M_3}\right) / \left(2M_1\right),$$

$$K_2 = 2b_1\left(z - d_2 - \sqrt{l_1^2 - y^2}\right), M_3 = \left(\left(d_1^2 - d_3^2\right) + 4\left(b_2 - a_1\right)^2\right)^2 - 16l_2^2\left(b_2 - a_1\right)^2 + 16d_3^2\left(b_2 - a_1\right)^2,$$

$$K_3 = l_2^2 - \left(x + a_2\right)^2 - b_1^2 - \left(z - d_2 - \sqrt{l_1^2 - y^2}\right)^2, E_2 = 2\left(d_4 + \sqrt{l_1^2 - y^2}\right) - 2M_4, K_1 = -2\left(x + a_2\right)b_1,$$

$$E_1 = a_2^2 + M_4^2 + l_1^2 - 2M_4\left(d_4 + \sqrt{l_1^2 - y^2}\right) + \left(d_4 + \sqrt{l_1^2 - y^2}\right)^2 - l_2^2.$$

Downloaded from https://www.cambridge.org/core. UNIVERSIDAD AUTONOMA METROPOLITANA, on 16 Nov 2026 at 18:24:25, subject to the Cambridge Core terms of use, available at https://www.cambridge.org/core/terms. https://doi.org/10.1017/S0263574726103774

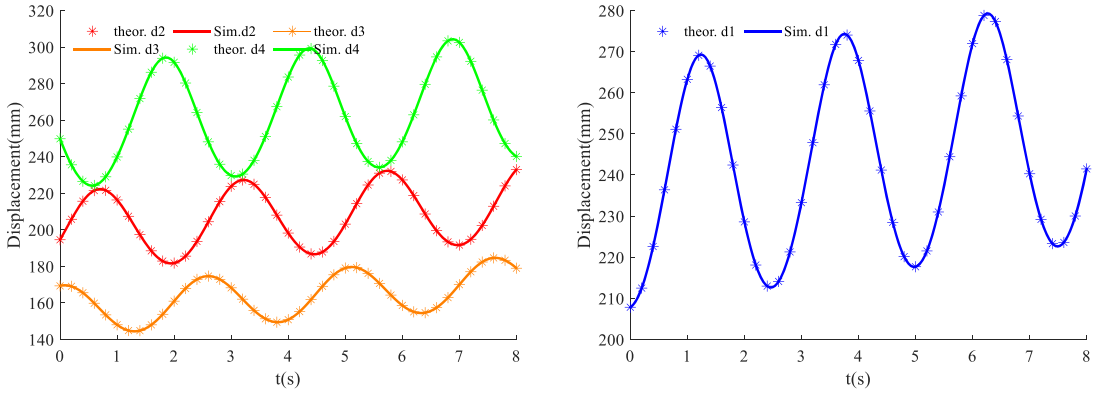


Figure 4. *Comparison of the driving joint displacements from theoretical and simulation results (a) d_2, d_3, and d_4 and (b) d_1.*

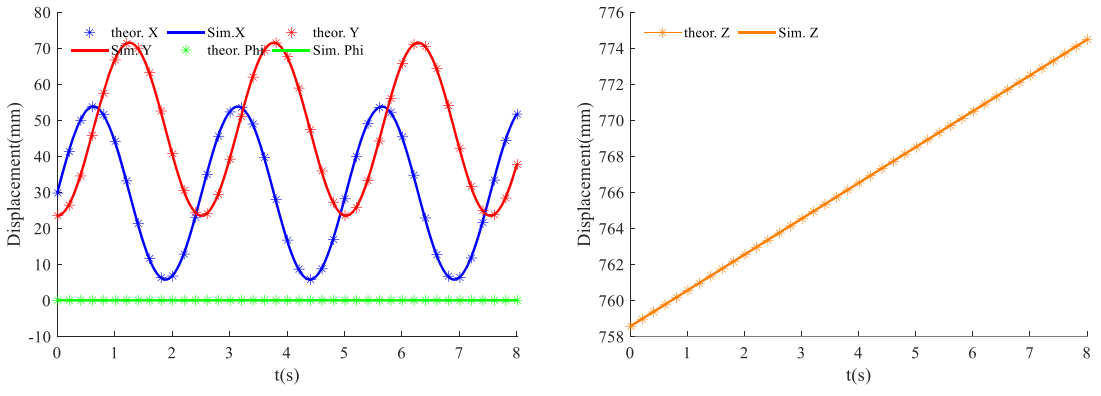


Figure 5. *Comparison between theoretical and simulated MP pose (a) x, y, and ϕ and (b) z.*

3.3. Calculation example of forward and inverse position solutions

The structural dimensions are given as $a_1 = a_2 = 306, l_1 = 308, l_2 = 342, b_1 = 110, b_2 = 90$ (unit: mm), and the initial pose of the MP is set to $(x_0, y_0, z_0, \varphi) = (29.765, 23.481, 758.559, 0)$. With the driving function in Eq. (19) applied at the preset pose of the MP, the theoretical solutions derived from Eq. (14) and the corresponding Adams simulation results are shown in Figure 4. Meanwhile, by inputting the corresponding data of the driving joints into Adams, the simulation curves of the pose of the MP in Adams and the theoretical solutions obtained via Eq. (18) are presented in Figure 5. Figures 4 and 5 show that the theoretical curves of the driving joints and the MP are almost the same as the corresponding simulation curves in Adams, which verifies the correctness of the kinematic analytical solutions of the improved 3T1R PM.

$$\begin{cases} x = x_0 + 24\sin(2.5t), y = y_0 + 24 - 24\cos(2.5t) \\ z = z_0 + \dfrac{12.5t}{2\pi}, \varphi = 0 \end{cases} \tag{19}$$

Downloaded from https://www.cambridge.org/core. UNIVERSIDAD AUTONOMA METROPOLITANA, on 16 Nov 2026 at 18:24:25, subject to the Cambridge Core terms of use, available at https://www.cambridge.org/core/terms. https://doi.org/10.1017/S0263574726103774

4. Velocity and singularity analysis

4.1. Velocity analysis

Velocity analysis is the basis of the singularity analysis. By differentiating both sides of Eq. (14), we can derive the mapping between the input velocity $\dot{d}_i (i = 1, 2, 3, 4)$and the output velocity $(\dot{x}, \dot{y}, \dot{z}, \dot{\phi})$. To date, numerous studies have investigated the Jacobian matrix of the mechanism in detail, such as Ref. [30–32]. Therefore, the derivation of the Jacobian matrix is omitted here. The derived Jacobian matrix can be expressed as follows:

$$\boldsymbol{J}_d \dot{\boldsymbol{d}} = \boldsymbol{J}_X \dot{\boldsymbol{X}} \tag{20}$$

The $\boldsymbol{J}_d$ and $\boldsymbol{J}_X$ are the inverse Jacobian matrix and the forward Jacobian matrix, respectively, and are given as follows:

$$\boldsymbol{J}_d = \begin{bmatrix} J_{d11} & 0 & 0 & 0 \\ 0 & J_{d22} & 0 & 0 \\ 0 & 0 & J_{d33} & 0 \\ 0 & 0 & 0 & J_{d44} \end{bmatrix} \tag{21}$$

$$\boldsymbol{J}_X = \begin{bmatrix} J_{X11} & J_{X12} & J_{X13} & J_{X14} \\ J_{X21} & J_{X22} & J_{X23} & J_{X24} \\ J_{X31} & J_{X32} & J_{X33} & J_{X34} \\ J_{X41} & J_{X42} & J_{X43} & J_{X44} \end{bmatrix} \tag{22}$$

where

$J_{d11} = \sin\theta_{11} \sin\theta_{12}, J_{d22} = \sin\theta_{21} \sin\theta_{22}, J_{d33} = \sin\theta_{31} \sin\theta_{32}, J_{d44} = \sin\theta_{41} \sin\theta_{42},$

$J_{X11} = \cos\theta_{11} \sin\theta_{12}, J_{X12} = \cos\theta_{12} \sin\theta_{11}, J_{X13} = \sin\theta_{11} \sin\theta_{12}, J_{X14} = 0, J_{X21} = \sin\theta_{21} \cos\theta_{22},$

$J_{X22} = \cos\theta_{21} \sin\theta_{22}, J_{X23} = \sin\theta_{21} \sin\theta_{22}, J_{X31} = \cos\theta_{31} \sin\theta_{32}, J_{X32} = -\cos\theta_{32} \sin\theta_{31},$

$J_{X34} = 0, J_{X24} = (b_1 \cos\phi \sin\theta_{21} \sin\theta_{22} + b_1 \sin\phi \sin\theta_{21} \cos\theta_{22}), J_{X33} = \sin\theta_{31} \sin\theta_{32},$

$J_{X41} = -\cos\theta_{42} \sin\theta_{41}, J_{X42} = \cos\theta_{41} \sin\theta_{42}, J_{X43} = \sin\theta_{41} \sin\theta_{42}, J_{X44} = 0$

When $|\boldsymbol{J}_d| \neq 0$, the Jacobian matrix for the improved PM 2PPaRR-2PPaRU equals

$$\boldsymbol{J} = \boldsymbol{J}_d^{-1} \boldsymbol{J}_X \tag{23}$$

4.2. Singularity analysis

Singularity is an inherent property of the PMs. It significantly affects the PM's performance, especially near its singular configuration, potentially causing damage to equipment. In this section, we will examine inverse kinematic singularity, forward kinematic singularity, and combined kinematic singularity [33].

4.2.1. Inverse kinematics singularity

Inverse kinematic singularity may arise when the MP is at the workspace boundary. In such a configuration, the MP loses one or more DOFs. When this occurs, $|\boldsymbol{J}_d| = 0$ and $|\boldsymbol{J}_x| \neq 0$. Since $\boldsymbol{J}_d$ is a diagonal matrix, it is easy to obtain $|\boldsymbol{J}_d| = 0$ when $\sin\theta_{i1} \sin\theta_{i2} = 0 (i = 1, 2, 3, 4)$. To avoid interference between the links, the following constraints should be satisfied:

$$\begin{cases} 30^\circ \leq \theta_{i1} \leq 150^\circ \\ 0 \leq \theta_{i2} < 90^\circ \end{cases} \tag{24}$$

From Eq. (24), the four situations can be found as follows:

$$\theta_{i2} = 0 \ (i = 1, 2, 3, 4) \tag{25}$$

In these situations, links $B_iC_i (i = 1, 2, 3, 4)$ and the MP are coplanar and parallel with the *XOY* plan when $\theta_{i2} = 0$; meanwhile, the MP lies on the boundary of its workspace. The four inverse kinematic singular configurations are presented in Figure 6.

Downloaded from https://www.cambridge.org/core. UNIVERSIDAD AUTONOMA METROPOLITANA, on 16 Nov 2026 at 18:24:25, subject to the Cambridge Core terms of use, available at https://www.cambridge.org/core/terms. https://doi.org/10.1017/S0263574726103774

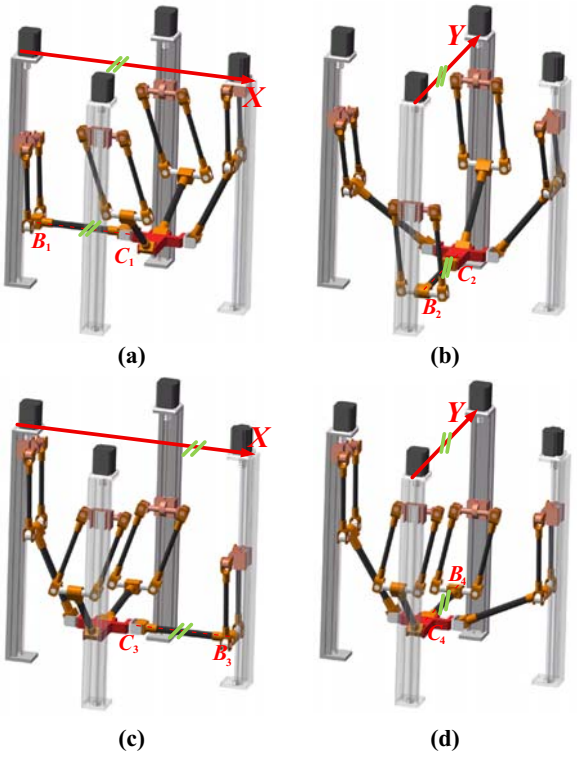


Figure 6. *The inverse kinematic singularity configurations (a) $\theta_{12} = 0$, (b) $\theta_{22} = 0$, (c) $\theta_{32} = 0$, and (d) $\theta_{42} = 0$.*

4.2.2. Forward kinematics singularity

A forward kinematic singularity, also known as a parallel singularity, occurs within the workspace. In such configurations, the MP undergoes infinitesimal motion in certain directions while the driving joints remain fixed, which implies that the MP obtains extra DOFs. The forward kinematic singularity occurs when $|\boldsymbol{J}_d| \neq 0$ and $|\boldsymbol{J}_X| = 0$. According to Eq. (22), $\det(\boldsymbol{J}_X) = -b_1 \sin\theta_{11} \sin\theta_{21} \sin\theta_{41} \sin(\phi + \theta_{22}) \sin(\theta_{12} + \theta_{32}) \sin(\theta_{42} + \theta_{31})$ can be obtained, the physical constraint is same as Eq. (24).

It can be obtained b_1, $\sin\theta_{11}$, $\sin\theta_{21}$ and $\sin\theta_{41}$ are not equal to 0. According to the forward kinematic singularity condition $|\boldsymbol{J}_d| \neq 0$, $|\boldsymbol{J}_X| = 0$ and Eq. (24), it can be easily derived that $\sin(\theta_{12} + \theta_{32}) \neq 0$. Thus, $|\boldsymbol{J}_X| = 0$ is equal to:

$$\sin(\theta_{42} + \theta_{31}) = 0 \text{ or } \sin(\phi + \theta_{22}) = 0 \tag{26}$$

When $\sin(\theta_{42} + \theta_{31}) = 0$, combined with the physical constraint $x_{C3} = x_{C4}$ (where x_{C3} and x_{C4} are the projections of the geometric centers of revolute joints C_3 and C_4 onto the $\boldsymbol{X}$-axis), the following equation can be obtained:

$$\begin{cases} \theta_{31} + \theta_{42} = \pi \\ l_1 \cos\theta_{31} = a_2 - l_2 \cos\theta_{42} \end{cases} \tag{27}$$

It can be derived from Eq. (27) that $\theta_{42} = a\cos(a_2/(l_2 - l_1))$, which means $l_2 - l_1 > a_2$. This will lead to an excessively long link B_iC_i $(i = 1, 2, 3, 4)$, reducing the PM's stiffness and rendering it impractical for control. When $\sin(\theta_{22} + \phi) = 0$, it can be derived that $\phi = -\theta_{22}$. In this singular configuration, the axis of link B_2C_2 is coplanar with the MP. Figure 7 presents one of the singular configurations associated with forward kinematics.

Downloaded from https://www.cambridge.org/core. UNIVERSIDAD AUTONOMA METROPOLITANA, on 16 Nov 2026 at 18:24:25, subject to the Cambridge Core terms of use, available at https://www.cambridge.org/core/terms. https://doi.org/10.1017/S0263574726103774

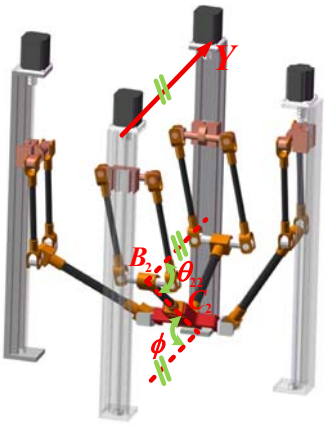


Figure 7. *The forward kinematic singularity configuration* $\theta_{22} = -\phi$.

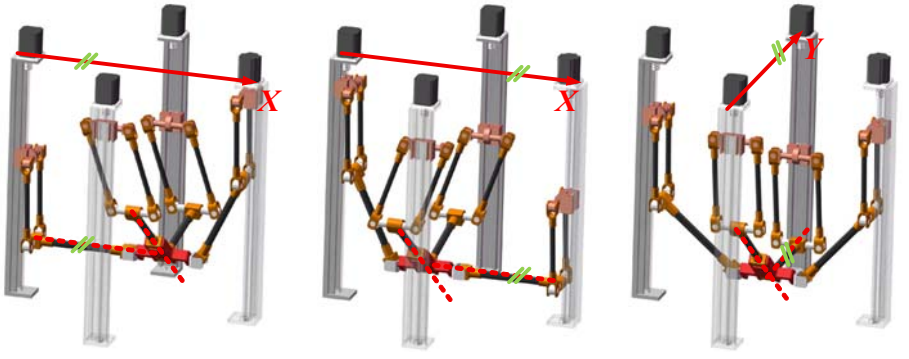


Figure 8. *Combined kinematic singular configurations (a)* $\theta_{22} = -\phi$ *and* $\theta_{12} = 0$, *(b)* $\theta_{22} = -\phi$ *and* $\theta_{32} = 0$, *and (c)* $\theta_{22} = -\phi$ *and* $\theta_{42} = 0$.

4.2.3. Combined kinematic singularity

In the combined kinematic singular configurations of the mechanism, the MP can move in one or several directions when the actuated joints are locked. Conversely, when the MP is constrained, the actuated joints can undergo finite motion. The corresponding conditions are $|\boldsymbol{J}_d| = 0$ and $|\boldsymbol{J}_X| = 0$. Based on the analysis in Sections 4.2.1 and 4.2.2, three types of combined singular configurations can be identified, as shown in Figure 8.

5. Motion/force transmission analysis and parameter optimization

5.1. Local motion/force transmission analysis

Liu et al. [22, 23] proposed the local transmission index (LTI) based on the transmission angle theory [34]. The transmission index reflects the energy transfer efficiency of the PM. The closer the transmission index is to unity, the higher the transmission efficiency. The LTI can be defined as follows:

$$\begin{cases} \mathrm{ITI}_i = \dfrac{|\$_{i1} \circ \$_{Ti}|}{|\$_{i1} \circ \$_{Ti}|_{\max}} \\ \mathrm{OTI}_i = \dfrac{|\$_{oi} \circ \$_{Ti}|}{|\$_{oi} \circ \$_{Ti}|_{\max}} \\ \mathrm{LTI} = \min\{\mathrm{ITI}_i, \mathrm{OTI}_i\} \end{cases} \tag{28}$$

Downloaded from https://www.cambridge.org/core. UNIVERSIDAD AUTONOMA METROPOLITANA, on 16 Nov 2026 at 18:24:25, subject to the Cambridge Core terms of use, available at https://www.cambridge.org/core/terms. https://doi.org/10.1017/S0263574726103774

where $\$_{i1}$, $\$_{Ti}$ and $\$_{Oi}$ denote the input twist screw, transmission wrench screw and the output twist screw of the limb i, respectively. ITI_i, OTI_i and LTI represent the input transmission index, output transmission index, and the minimum value of all the input and output transmission index, that is, the LTI of the PM. LTI ranges from zero to unity, and a higher LTI indicates better transmissibility.

Fixing $\$_{i1}$ (the input twist screw), the newly added constraint wrench screw represents the transmission wrench screw of limb i. According to the reciprocity between the twist screw system and the wrench screw system [35], we can obtain the transmission wrench screws in limbs 1, 2, 3, and 4 as follows (see Appendix A):

$$\begin{cases} \$_{T1} = (l_{11}, m_1, n_1; p_1, q_1, r_1) \\ \$_{T2} = (l_{21}, m_2, n_2; p_2, q_2, r_2) \\ \$_{T3} = (l_{31}, m_3, n_3; p_3, q_3, r_3) \\ \$_{T4} = (l_{41}, m_4, n_4; p_4, q_4, r_4) \end{cases} \tag{29}$$

With the input joint in limb i actuated and the input joints in the other three limbs fixed, the unit twist screw of the MP is equivalent to the output twist screw of that limb. According to the reciprocity between the twist screw $\$_{Oi}(i = 1 \sim 4)$ and the wrench screw $\$_{Ci}, \$_{Tk}(i = 1, 2; k = 1 \sim 4)$:

$$\$_{Oi} \circ \$_{Ci} = 0, \$_{Oi} \circ \$_{Tk} = 0 \ (i \neq k) \tag{30}$$

The PM's output twist screws can be determined. As indicated by the analysis in Ref. [12], it is evident that the cross-section profile of the mechanism's reachable workspace remains consistent at different heights when the orientation of the MP is fixed, without accounting for the limitations of actuated displacements. Therefore, this section focuses on analyzing the distribution of LTI within the cross-section of the workspace at a specific operating height ($Z = 1{,}000$ mm). Given that the 3T1R PM is primarily used in light-load scenarios, the configuration of the improved 3T1R PM is picked into GTW when $\mathrm{LTI} \geq 0.5$. The structural parameters remain consistent with those in Section 3.3. The LTI distribution across the reachable workspace under various orientations is symmetrical about the $\boldsymbol{X}$-axis, as depicted in Figure 9, aligning with the symmetry of the mechanism architecture about the $\boldsymbol{X}$-axis. Compared to the LTI distribution of the original design in Ref. [12], the region with poor transmission performance is deviated from the home configuration.

5.2. Overall good transmission workspace analysis

To provide an overall measure of the good transmission region within the entire reachable workspace, the GTWR [36] is defined as follows:

$$\Gamma = \frac{\int \gamma ds}{\int ds} \tag{31}$$

Here, γ refers to the point in the GTW, $\int \gamma ds$ refers to the set of γ in the overall reachable workspace and $\int ds$ refers to the total discrete points in the reachable workspace. The overall reachable workspace comprises the cross-sections obtained under various orientations at the operating height $Z = 1{,}000$ mm. Clearly, Γ ranges from 0 to 1, with higher values indicating better global transmission performance. In Figure 9, the 3T1R PM exhibits GTW only when the orientation of the MP equals 0 and 45°, resulting in GTWR values of 0.223 and 0.239, respectively.

6. Stiffness analysis of the 2PPaRR-2PPaRU PM

The stiffness performance reflects the ability of a PM to resist deflection under external loads, which is a crucial index for evaluating the accuracy of the PM. In this section, the VJM [24–27] is applied to derive the stiffness model of the 2PPaRR-2PPaRU PM. The stiffness of the actuators, parallelogram links, and $B_iC_i(i = 1, 2, 3, 4)$ links, together with the deflections of the passive joints, is taken into account.

Downloaded from https://www.cambridge.org/core. UNIVERSIDAD AUTONOMA METROPOLITANA, on 16 Nov 2026 at 18:24:25, subject to the Cambridge Core terms of use, available at https://www.cambridge.org/core/terms. https://doi.org/10.1017/S0263574726103774

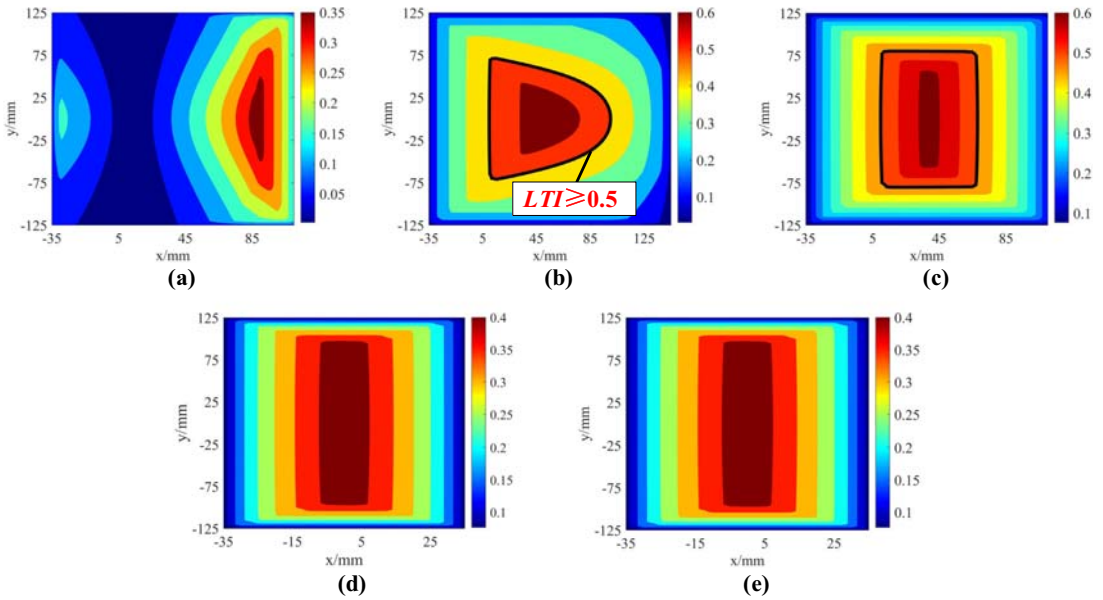


Figure 9. *LTI distribution (a) $\phi = -45°$, (b) $\phi = 0$, (c) $\phi = 45°$, (d) $\phi = -90°$, and (e) $\phi = 90°$.*

6.1. Stiffness matrix of the parallelogram

Since the links are slender and flexible, they can be modeled as cantilever beams in the stiffness analysis. Based on the Euler–Bernoulli equation [37], the stiffness matrix of a link can be derived as:

$$\boldsymbol{K}_{bar} = \begin{bmatrix} k_{11} & 0 & 0 & 0 & 0 & 0 \\ 0 & k_{22} & 0 & 0 & 0 & k_{26} \\ 0 & 0 & k_{33} & 0 & k_{35} & 0 \\ 0 & 0 & 0 & k_{44} & 0 & 0 \\ 0 & 0 & k_{53} & 0 & k_{55} & 0 \\ 0 & k_{62} & 0 & 0 & 0 & k_{66} \end{bmatrix} \tag{32}$$

where $k_{11} = GI_x/l_i,\ k_{22} = 4EI_y/l_i,\ k_{33} = 4EI_z/l_i,\ k_{44} = EA/l_i,\ k_{55} = 12EI_z/l_i^3,\ k_{66} = 12EI_y/l_i^3, k_{26} = k_{62} = 6EI_y/l_i^2, k_{35} = k_{53} = -6EI_z/l_i^2$. The l_i is the link length, A, E and G are the cross-section area, the Young's and shear modules of the link, I_y, I_z and I_x are the quadratic and polar moments of inertia of the cross section, respectively.

The virtual spring model of the parallelogram structure is shown in Figure 10. The elastic deformations of the upper link are equivalent to the elastic deformations of the virtual spring at the end of the link, and the motion of the passive joints R1, R3 is considered. The elastic deformation $\delta \boldsymbol{t}^{up}$ of the end of the upper limb equals:

$$\delta \boldsymbol{t}^{up} = \boldsymbol{J}_{\Pi}^{\theta} \delta \boldsymbol{\theta}_{\Pi} + \boldsymbol{J}_{\varphi}^{up} \delta \boldsymbol{q}_{\Pi} \tag{33}$$

where $\boldsymbol{J}_{\Pi}^{\theta}$ is the Jacobian matrix that corresponds to the deflection $\delta \boldsymbol{\theta}_{\Pi}$ of the upper link, and $\boldsymbol{J}_{\varphi}^{up}$ is the Jacobian matrix that corresponds to the motion of the passive revolute joints $\delta \boldsymbol{q}_{\Pi}$. The $\boldsymbol{J}_{\Pi}^{\theta}$ and $\boldsymbol{J}_{\varphi}^{up}$ are expressed as:

Downloaded from https://www.cambridge.org/core. UNIVERSIDAD AUTONOMA METROPOLITANA, on 16 Nov 2026 at 18:24:25, subject to the Cambridge Core terms of use, available at https://www.cambridge.org/core/terms. https://doi.org/10.1017/S0263574724103774

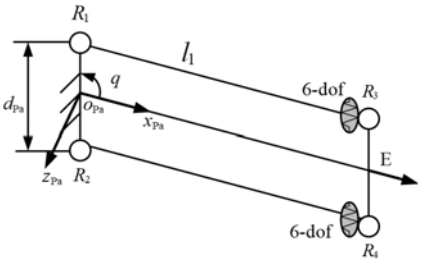


Figure 10. *The virtual spring model of the parallelogram.*

$$\boldsymbol{J}_{\Pi}^{\theta}=\begin{bmatrix} 1 & 0 & 0 & 0 & 0 & 0 \\ 0 & 1 & 0 & 0 & 0 & 0 \\ 0 & 0 & 1 & 0 & 0 & 0 \\ 0 & dSq/2 & 0 & 1 & 0 & 0 \\ -dSq/2 & 0 & -L-dCq/2 & 0 & 1 & 0 \\ 0 & L+dCq/2 & 0 & 0 & 0 & 1 \end{bmatrix},\ \boldsymbol{J}_{\varphi}^{up}=\begin{bmatrix} 0 & 0 \\ 1 & 1 \\ 0 & 0 \\ dSq/2 & dSq/2 \\ 0 & 0 \\ dCq/2 & L+dCq/2 \end{bmatrix} \tag{34}$$

where $Sq=\sin q$, $Cq=\cos q$. According to the static equilibrium equation [25]:

$$\begin{bmatrix} \boldsymbol{J}_{\Pi}^{\theta}\boldsymbol{K}_{bar}^{-1}\boldsymbol{J}_{\Pi}^{\theta T} & \boldsymbol{J}_{\varphi}^{up} \\ \boldsymbol{J}_{\varphi}^{upT} & \boldsymbol{0}_{2\times 2} \end{bmatrix}\begin{bmatrix} \boldsymbol{f}_{up} \\ \delta\boldsymbol{\varphi}^{up} \end{bmatrix}=\begin{bmatrix} \delta\boldsymbol{t}^{up} \\ \boldsymbol{0}_{n\times n} \end{bmatrix} \tag{35}$$

The stiffness matrix of the upper limb is:

$$\boldsymbol{K}_{\Pi}^{up}=\begin{bmatrix} \boldsymbol{J}_{\Pi}^{\theta}\boldsymbol{K}_{bar}^{-1}\left(\boldsymbol{J}_{\Pi}^{\theta}\right)^{T} & \boldsymbol{J}_{\varphi}^{up} \\ \left(\boldsymbol{J}_{\varphi}^{up}\right)^{T} & \boldsymbol{0}_{2\times 2} \end{bmatrix}^{-1} \tag{36}$$

The stiffness matrix $\boldsymbol{K}_{\Pi}^{up}$ of the upper limb is the first six-dimensional entry extracted from Eq. (36). Due to the passive joints' motion compensation, the translational stiffness along the $z_{Pa}-$ axis vanishes, and the stiffness matrix of the parallelogram structure can be represented by the first 5-dimensional submatrix as follows:

$$\boldsymbol{K}_{\Pi}^{up}=\begin{bmatrix} k_{11}+k_{55}d^2S_q^2/4 & 0 & k_{55}d^2S_{2q}/8 & 0 & 0 \\ 0 & k_{44}d^2S_q^2/4 & 0 & 0 & 0 \\ k_{55}d^2S_{2q}/8 & 0 & k_{33}+k_{55}d^2C_q^2/4 & 0 & k_{35} \\ 0 & 0 & 0 & k_{44} & 0 \\ 0 & 0 & k_{35} & 0 & k_{55} \end{bmatrix}_{5\times 5} \tag{37}$$

where k_{ij} denotes the (i,j) entry of the matrix $\boldsymbol{K}_{\Pi}^{up}$. Similarly, the stiffness matrix of the lower limb can be obtained. The overall stiffness matrix of the parallelogram structure equals:

$$\boldsymbol{K}_{\Pi}=\boldsymbol{K}_{\Pi}^{up}+\boldsymbol{K}_{\Pi}^{down}=2\boldsymbol{K}_{\Pi}^{up} \tag{38}$$

6.2. Stiffness modeling of the PM

The 3T1R PM 2PPaRR-2PPaRU consists of two PPaRR limbs and two PPaRU limbs. Before establishing the stiffness matrix of the PM, the stiffness matrices of the two different types of limbs should be built first. The stiffness matrix of the PM is equivalent to the sum of the stiffness matrices of all four limbs.

Downloaded from https://www.cambridge.org/core. UNIVERSIDAD AUTONOMA METROPOLITANA, on 16 Nov 2026 at 18:24:25, subject to the Cambridge Core terms of use, available at https://www.cambridge.org/core/terms. https://doi.org/10.1017/S0263574726103774

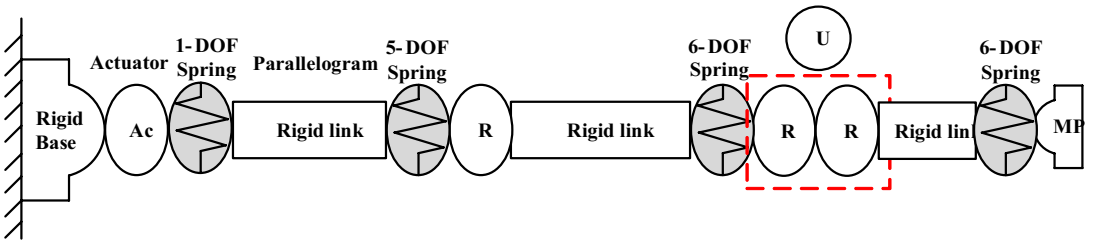


Figure 11. *The virtual spring model of the PPaRU limb.*

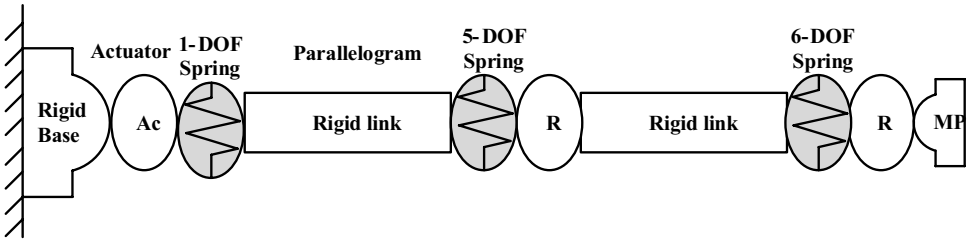


Figure 12. *The virtual spring model of the PPaRR limb.*

6.2.1. Stiffness modeling of the PPaRU limb

The virtual spring model of the PPaRU limb is presented in Figure 11, where a 1-DOF virtual spring denotes the actuator stiffness, while a 5-DOF and two 6-DOF virtual springs correspond to the stiffness of the parallelogram structure, the B_iC_i and the $U_i(i = 1, 3)$ links, respectively.

According to the static equilibrium equation:

$$\begin{bmatrix} \boldsymbol{J}_{\theta}^{i}\left(\boldsymbol{K}_{Li}^{i}\right)^{-1}\left(\boldsymbol{J}_{\theta}^{i}\right)^{T} & \boldsymbol{J}_{q}^{i} \\ \left(\boldsymbol{J}_{q}^{i}\right)^{T} & \boldsymbol{0}_{4\times4} \end{bmatrix} \begin{bmatrix} \boldsymbol{f} \\ \delta\boldsymbol{q}_i \end{bmatrix} = \begin{bmatrix} \boldsymbol{K}_{Li} & * \\ * & * \end{bmatrix} \begin{bmatrix} \boldsymbol{f} \\ \delta\boldsymbol{q}_i \end{bmatrix} = \begin{bmatrix} \delta\boldsymbol{t}_{Li} \\ \boldsymbol{0} \end{bmatrix} \tag{39}$$

The stiffness matrix of the PPaRU limb is the first 6×6 submatrix extracted from the following matrix:

$$\boldsymbol{K}_{Li} = \begin{bmatrix} \boldsymbol{J}_{\theta}^{i}\left(\boldsymbol{K}_{Li}^{i}\right)^{-1}\left(\boldsymbol{J}_{\theta}^{i}\right)^{T} & \boldsymbol{J}_{q}^{i} \\ \left(\boldsymbol{J}_{q}^{i}\right)^{T} & \boldsymbol{0}_{4\times4} \end{bmatrix}^{-1} \tag{40}$$

where $\boldsymbol{K}_{Li}(i = 1, 3)$ is the stiffness matrix of the PPaRU limb, $\boldsymbol{f}$ is the force applied at the free end of the limb, $\delta\boldsymbol{q}_i$ is the motion of passive joints, $\boldsymbol{K}_{Li}^{i} = diag(\mathrm{K}_{ac}, \boldsymbol{K}_{Pa}, \boldsymbol{K}_{rod1}, \boldsymbol{K}_{rod2})$ represents the stiffness in the joint space, $\boldsymbol{J}_{q}^{i} = (\$_{q1}^{i}\ \$_{q2}^{i}\ \$_{q3}^{i}\ \$_{q4}^{i})$ is the Jacobian matrix of the passive joints, $\boldsymbol{J}_{\theta}^{i} = (\$_{ac}\ \$_{Pa1}^{i}\ \$_{Pa2}^{i} \ldots \$_{Rod12}^{i})$ is the Jacobian matrix of the links (see Appendix B), $\boldsymbol{r}_{C1} = (x, y - b2 + l_u, z)$ and $\boldsymbol{r}_{C3} = (x, y + b2 - l_u, z)$ are the end points of the U_1 and U_3 joints, respectively.

6.2.2. Stiffness modeling of the PPaRR limb

The virtual spring model of the PPaRR limb is presented in Figure 12, where the 1-DOF virtual spring denotes the stiffness of the actuator, and the 5-DOF and 6-DOF virtual springs represent the stiffness of the Pa joint and the link, respectively.

Similarly, the stiffness matrix of the PPaRR limb is the first 6×6 submatrix extracted from the following matrix:

$$\boldsymbol{K}_{Li} = \begin{bmatrix} \boldsymbol{J}_{\theta}^{i}\left(\boldsymbol{K}_{Li}^{i}\right)^{-1}\left(\boldsymbol{J}_{\theta}^{i}\right)^{T} & \boldsymbol{J}_{q}^{i} \\ \left(\boldsymbol{J}_{q}^{i}\right)^{T} & \boldsymbol{0}_{3\times3} \end{bmatrix} \tag{41}$$

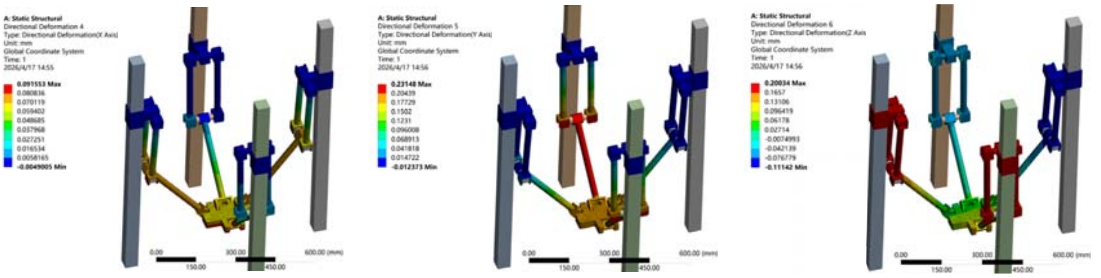
Downloaded from https://www.cambridge.org/core. UNIVERSIDAD AUTONOMA METROPOLITANA, on 16 Nov 2026 at 18:24:25, subject to the Cambridge Core terms of use, available at https://www.cambridge.org/core/terms. https://doi.org/10.1017/S0263574726103774

Table II. *The cross-sectional area of the links and material properties*

K_{ac}/N/m	E/MPa	r_1/mm	r_u/mm	l_u/mm	d_{Pa}/mm	Poisson ratio/μ
5e4	2e5	12	11	28	110	0.3

Table III. *The result comparison of the FEA model and the analytical model of the PM*

	δx(mm)	δy(mm)	δz(mm)
Analytical solutions	0.0746	0.1969	0.0380
FEA solutions	0.0770	0.1993	0.0388
Relative error (%)	3.12	1.20	2.06



(a) **(b)** **(c)**

Figure 13. *FEA model of the 2PPaRR-2PPaRU PM. (a) Linear deformation along the x-axis, (b) linear deformation along the y-axis, and (c) linear deformation along the z-axis.*

where $\boldsymbol{K}_{Li}(i=2,4)$ is the stiffness matrix of the PPaRR limb, $\boldsymbol{K}_{Li}^{i} = diag(\mathrm{K}_{ac}, \boldsymbol{K}_{Pa}, \boldsymbol{K}_{rod})$ represents the stiffness matrix in the joint space, $\boldsymbol{J}_{q}^{i} = (\$_{q1}^{i}\ \$_{q2}^{i}\ \$_{q3}^{i})$ is the Jacobian matrix of the passive joints and $\boldsymbol{J}_{\theta}^{i} = (\$_{ac}\ \$_{Pa1}^{i}\ \$_{Pa2}^{i} \ldots \$_{Rod5}^{i}\ \$_{Rod6}^{i})$ is the Jacobian matrix of the links (see Appendix B).

The overall stiffness matrix $\boldsymbol{K}$ of the 3T1R PM is

$$\boldsymbol{K} = \boldsymbol{K}_{L1} + \boldsymbol{K}_{L2} + \boldsymbol{K}_{L3} + \boldsymbol{K}_{L4} \tag{42}$$

6.3. Simulation case

The structural parameters are the same as those in Section 3.3. Table II lists the cross-sectional radius of the links and material properties of the 2PPaRR-2PPaRU PM, where K_{ac} denotes the stiffness of the actuator, r_1 denotes the link radius, and r_u denotes the radius of the U joint. To verify the correctness of the stiffness model of the PM, an external force $\boldsymbol{f} = (1\mathrm{N.m}; 1\mathrm{N.m}; 1\mathrm{N.m}; 12\mathrm{N}; 12\mathrm{N}; 12\mathrm{N})$ is applied to the MP at the given pose (34.417 mm, 8.211mm, 838.575 mm, 0). The results of the finite element model (FEM) and the analytical results are shown in Table III, and Figure 13 presents the deformation of the PM. The absolute values of the relative errors between the FEM results and the theoretical results in Table III are within 5%, which validates the correctness of the theoretical model.

6.4. The stiffness performance analysis of the 2PPaRR-2PPaRU

The stiffness performance of the PM is correlated with its configuration. Similar to the kinematic indices based on the Jacobian matrix, the typical index based on the stiffness matrix has unclear physical significance for the unit inconsistency of the rotational stiffness and translational stiffness [28]. The virtual stiffness index (VSI) [28] reflects the stiffness of a PM in terms of energy, which is used to evaluate the

Downloaded from https://www.cambridge.org/core. UNIVERSIDAD AUTONOMA METROPOLITANA, on 16 Nov 2026 at 18:24:25, subject to the Cambridge Core terms of use, available at https://www.cambridge.org/core/terms. https://doi.org/10.1017/S0263574726103774

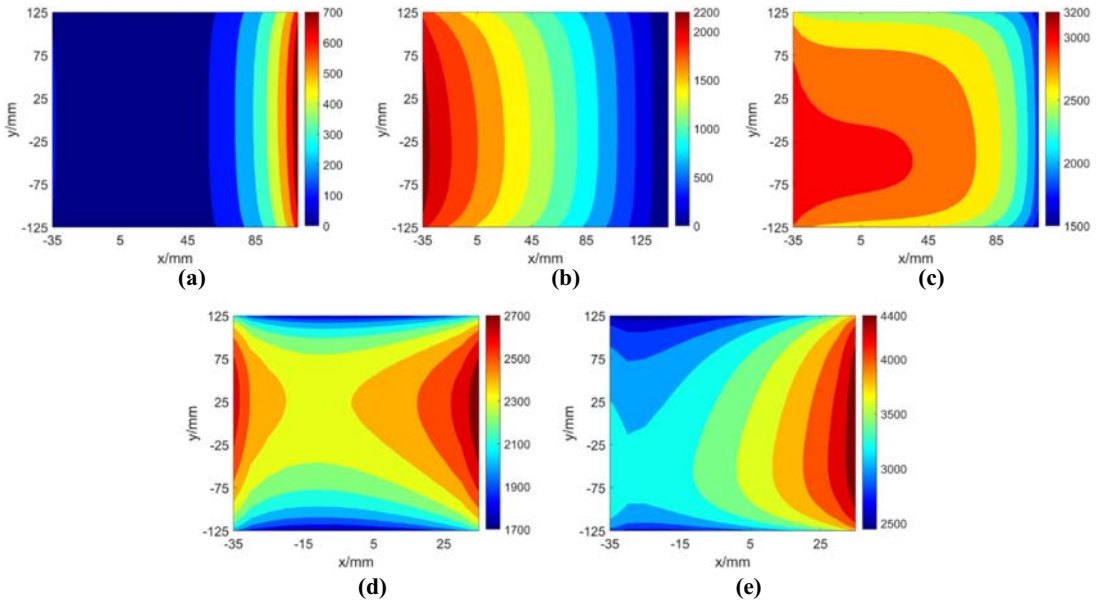


Figure 14. *The VSI distribution over the reachable workspace under different orientations. (a) $\phi = -45°$, (b) $\phi = 0$, (c) $\phi = 45°$, (d) $\phi = -90°$, and (e) $\phi = 90°$.*

local stiffness of the PM. When a force $\boldsymbol{f}$ is applied to the origin of the MP, the virtual work $W_V$can be written as:

$$W_V = \boldsymbol{f}^T \delta \boldsymbol{t} \tag{43}$$

where $\delta \boldsymbol{t}$ is the virtual displacement vector caused by the force $\boldsymbol{f}$. Substituting $\delta \boldsymbol{t} = \boldsymbol{K}^{-1}\boldsymbol{f}$ into Eq. (43), the virtual work can be rewritten as

$$VW = \frac{1}{\boldsymbol{f}^T \boldsymbol{K}^{-1} \boldsymbol{f}} \tag{44}$$

Within the linear elastic range, the relationship between virtual displacement and the force $\boldsymbol{f}$ satisfies Hooke's law. Under a certain external force, a larger $\boldsymbol{f}^T\boldsymbol{K}^{-1}\boldsymbol{f}$ corresponds to larger virtual deflections and virtual work, thus indicating poor stiffness performance, and vice versa. Because the stiffness index is closely related to the direction of the wrench applied on the MP [28], the stiffness performance distribution of the 2PPaRR-2PPaRU over the reachable workspace under a unit force $\boldsymbol{f} = (\sqrt{6}/6\text{N.m};\sqrt{6}/6\text{N.m};\sqrt{6}/6\text{N.m};\sqrt{6}/6\text{N};\sqrt{6}/6\text{N};\sqrt{6}/6\text{N})$ is presented in Figure 14. It can be seen from Figure 14 that the stiffness performance of the PM with $\phi = 45°$ and $90°$ is better than that of the PM with $\phi = -45°$ and $-90°$, demonstrating that the PM exhibits higher stiffness performance when ϕ is positive.

7. Parameter optimization design

The performance of the PM is significantly influenced by its structural parameters. To optimize the size of the mechanism, the parameter-finiteness normalization method (PFNM) [38, 39] is employed. Unlike other optimization methods like Genetic Algorithm, PFNM yields multiple sets of structural parameters with similar performance in a single calculation. This approach allows designers to flexibly adjust parameters based on specific requirements, saving time. However, expressing the six structural

Downloaded from https://www.cambridge.org/core. UNIVERSIDAD AUTONOMA METROPOLITANA, on 16 Nov 2026 at 18:24:25, subject to the Cambridge Core terms of use, available at https://www.cambridge.org/core/terms. https://doi.org/10.1017/S0263574726103774

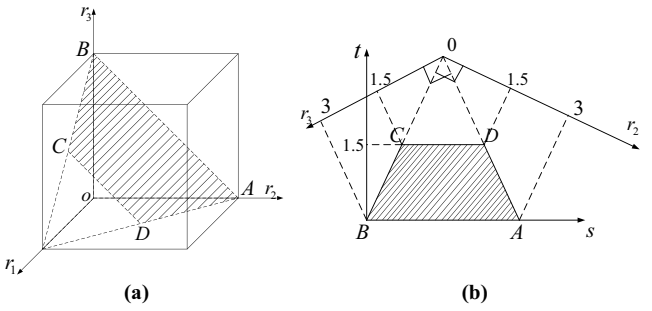


Figure 15. *Parameter design space model. (a) Spatial view and (b) plan view.*

parameters $(a_1, a_2, l_1, l_2, b_1, b_2)$ in 3D design space can be challenging. Thus, by defining $l_1 = l_2, a_1 = a_2, b_1 = 2b_2$, the three design variables can be obtained and normalized as:

$$\begin{cases} D = \dfrac{r_1 + r_2 + r_3}{3} \\ r_1 = b_2, r_2 = l_2, r_3 = a_1 \end{cases} \tag{45}$$

where D is a normalized factor and equals 340 mm. In real applications, the following conditions should be satisfied:

$$\begin{cases} r_1, r_2, r_3 \leq 3 \\ r_1 \leq r_3 \end{cases} \tag{46}$$

Following the procedures outlined in Refs. [38, 39], the parameter design space (PDS) can be established as shown in Figure 15(a). The trapezoid ABCD in Figure 15(a) represents all possible solutions. For convenience, the trapezoidal PDS ABCD is transformed into a plan view, as shown in Figure 15(b), where the relationship between the design parameters (r_1, r_2, r_3) in three-dimensional space and those (s, t) in plan space is given as follows:

$$\begin{cases} r_1 = t \\ r_2 = \dfrac{\sqrt{3}}{2}s - \dfrac{t}{2} \\ r_3 = 3 - \dfrac{\sqrt{3}}{2}s - \dfrac{t}{2} \end{cases} \quad \text{or} \quad \begin{cases} s = \sqrt{3} + \dfrac{\sqrt{3}}{3}r_2 - \dfrac{\sqrt{3}}{3}r_3 \\ t = r_1 \end{cases} \tag{47}$$

To ensure the correct assembly and motion of the mechanism, the design parameters in the trapezoid ABCD should also satisfy the following conditions:

$$\begin{cases} 2l_2 + 2b_2 \geq 2.2a_1 \\ 2l_2 + b_1 \geq 2.2a_2 \end{cases} \tag{48}$$

Maintaining a balance among various performance indices is essential to avoid sacrificing one index for another. To achieve this, the ORWA, GTWR, and GSI are jointly evaluated at $Z = 1{,}000$ mm. Their respective distributions over the PDS are shown in Figure 16(a)–(c). The results show that the ORWA decreases with the increase in t, while the GTWR achieves a high value in the middle region and the GSI decreases with the increase in s. To ensure that the PM exhibits satisfactory ORWA, motion/force transmission performance, and stiffness performance, the optimal region is derived by imposing the following constraints: ORWA ≥ 0.8, GTWR ≥ 0.25, and GSI ≥ 2400, as presented in Figure 16(d). This method provides multiple sets of design parameter selections. Subsequently, nine groups of data points are selected from Figure 16(d) as listed in Table IV. Among them, the design parameters of Group 7 are chosen as the optimal results, and the CAD model of the optimized 3T1R PM is shown in Figure 17.

Downloaded from https://www.cambridge.org/core. UNIVERSIDAD AUTONOMA METROPOLITANA, on 16 Nov 2026 at 18:24:25, subject to the Cambridge Core terms of use, available at https://www.cambridge.org/core/terms. https://doi.org/10.1017/S0263574726103774

Table IV. *The ORWA, GTWR, and GSI in the PDS*

Group	s	t	r_1	r_2	r_3	a_1	l_2	b_1	ORWA(10^5)	GTWR	GSI
			0.206	0.906	1	340	308	110	2.3	0.1191	1784.
1	1.9	0.4	0.4	1.445	1.155	393	491	272	11.092	0.3201	10, 227.0
2	2.05	0.45	0.45	1.550	1.0	340	527	306	10.989	0.5067	10, 177.1
3	2.075	0.4	0.4	1.597	1.003	341	543	272	13.161	0.4952	7, 974.8
4	1.95	0.3	0.3	1.539	1.161	395	523	204	11.385	0.2961	4, 697.8
5	2.025	0.35	0.35	1.579	1.071	364	537	238	15.533	0.4362	6, 330.6
6	2.125	0.3	0.3	1.690	1.010	343	575	204	17.542	0.4040	3, 953.5
7	1.875	0.5	0.5	1.374	1.126	383	467	340	10.191	0.4259	17, 773.6
8	1.925	0.55	0.55	1.392	1.058	360	473	374	8.435	0.5255	17, 408
9	1.975	0.5	0.5	1.460	1.040	353	497	340	9.953	0.5475	13, 841.4

Note: All structural parameters are in mm. To align with the unit (m^2) in Fig. 16(a), all ORWA entries in Table IV must be divided by 10^6. For illustration, the ORWA of the first group (1,109,200) reduces to 1.1092 when divided by 10^6, matching the corresponding value in Fig. 16(a).

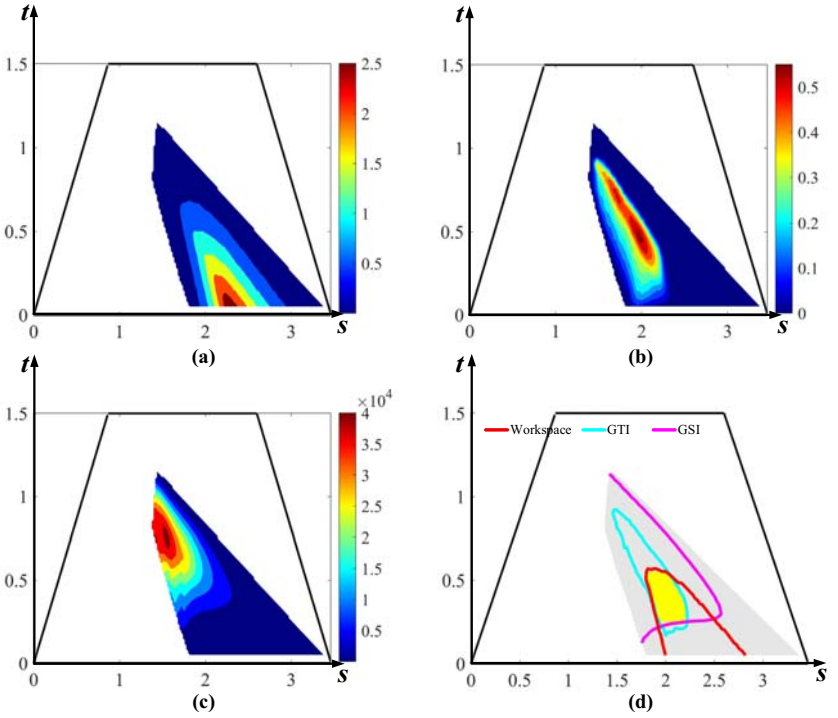


Figure 16. *ORWA, GTWR, and GSI distribution in the PDS. (a) distribution of ORWA, (b) distribution of GTWR, (c) distribution of GSI, and (d) optimum region.*

Group * represents the original structural parameters. The LTI and VSI distributions for the optimized parameters within the reachable workspace are shown in Figures 18 and 19, respectively. The GTWR values in Figure 18 are 0.736, 0.622, 0.0, 0.229, 0.229 for MP orientations of 0°, 45°, −45°, 90°, and −90°, respectively. Compared to the LTI distribution before optimization in Figure 9, which exhibits GTWR values of 0.223 and 0.239 for MP orientations of 0° and 45°, the optimized distribution yields notable improvements in both GTWR and ORWA. Furthermore, as shown in Figure 19, the GSI values of the optimized design are 22,671.3, 27,870.4, 3,070.8, 26,869.1, and 9,361.6 for the same sequence of MP orientations. Under these optimized parameters, the proportion of the workspace with good VSI reaches 1.0 for all MP orientations except −45°, where it accounts for 0.490. In contrast, the initial design

Downloaded from https://www.cambridge.org/core. UNIVERSIDAD AUTONOMA METROPOLITANA, on 16 Nov 2026 at 18:24:25, subject to the Cambridge Core terms of use, available at https://www.cambridge.org/core/terms. https://doi.org/10.1017/S0263574726103774



Figure 17. *The optimized 3T1R PM.*

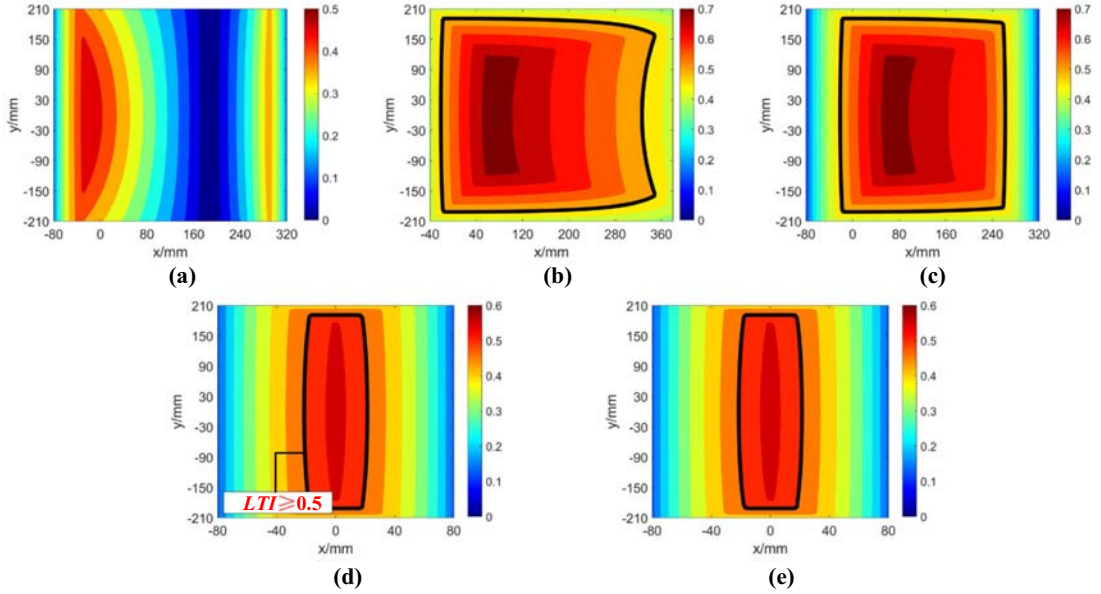


Figure 18. *LTI distribution in group 7 (a) $\phi = -45°$, (b) $\phi = 0$, (c) $\phi = 45°$, (d) $\phi = -90°$, and (e) $\phi = 90°$.*

produces much lower GSI values of 1,156.4, 2,707.5, 146.8, 3,513.7, and 2,344.3, and workspace regions with good VSI are only available at MP orientations of 45°, 90°, −90°, with corresponding fractions of 0.827, 1.0, and 0.390, respectively. This comparison validates the effectiveness of the optimization approach for the improved 3T1R PM.

8. Conclusions

This paper introduces an enhanced single MP 3T1R PM, denoted as 2PPaRR-2PPaRU, which incorporates decoupled rotational pitch motion. Building upon the original design, this improved version features coaxially connected end joints in limbs 1, 3, and 4, effectively addressing performance issues in the initial configuration. Furthermore, it ensures that the rotation of the MP is solely influenced by

Downloaded from https://www.cambridge.org/core. UNIVERSIDAD AUTONOMA METROPOLITANA, on 16 Nov 2026 at 18:24:25, subject to the Cambridge Core terms of use, available at https://www.cambridge.org/core/terms. https://doi.org/10.1017/S0263574726103774

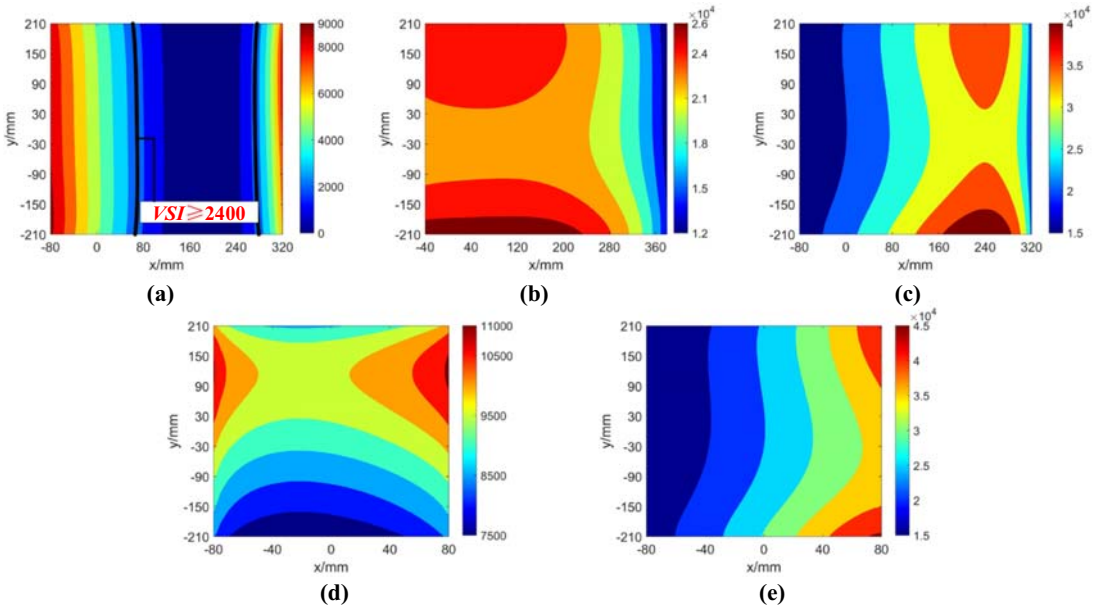


Figure 19. *VSI distribution in group 7 (a) $\phi = -45°$, (b) $\phi = 0$, (c) $\phi = 45°$, (d) $\phi = -90°$, and (e) $\phi = 90°$.*

limb 2, offering the advantage of partial motion decoupling. The paper presents both inverse and forward kinematic solutions, which are helpful to simplify kinematic analysis and real-time control efforts. Singularity analysis reveals that the improved 3T1R PM 2PPaRR-2PPaRU exhibits inverse, forward, and combined singularities. The LTI analysis shows that the poor performance at the initial configuration was removed. The stiffness analysis demonstrates that the region exhibiting higher stiffness is close to the workspace boundary under the given unit wrench. Finally, the multi-objective optimization results reveal significant improvements in the ORWA, GTWR, and GSI compared to the original design. These analyses establish a solid foundation for prototype manufacturing and motion planning in subsequent work.

Author contributions. Xiaoshu Zhang: Methodology, Software, Validation, Writing – original draft, Writing – review and editing, Conceptualization. Aihong Ji: Methodology, Supervision, Funding acquisition. Shikun Wen: Software, Investigation. Andong Jiang: Review & editing, Investigation. Yi Sun: Formal analysis. Zhikang Yang: Writing & editing, Visualization. Qian Qi: Visualization.

Financial support. This work was financially supported by the Special Funds for Science and Technology Programs in Jiangsu Province (BZ2024021), the National Natural Science Foundation of China (No. 52575339, No. 52575123), and the Natural Science Foundation of Jiangsu Province (BK20241407).

Competing interests. The authors declare no conflicts of interest exist.

Ethical approval. Not applicable.

References

[1] C. Lee and J. Hervé, "Type synthesis of primitive Schoenflies-motion generators," *Mech. Mach. Theory* **44**(10), 1980–1997 (2009).
[2] P. Richard, C. Gosselin and X. Kong, "Kinematic analysis and prototyping of a partially decoupled 4-DOF. 3T1R parallel manipulator," *J. Mech. Des*. **129**(6), 611–616 (2007).
[3] S. Guo, W. Ye, H. Qu, D. Zhang and Y. Fang, "A serial of novel four degrees of freedom parallel mechanisms with large rotational workspace," *Robotica* **34**(4), 764–776 (2016).

Downloaded from https://www.cambridge.org/core. UNIVERSIDAD AUTONOMA METROPOLITANA, on 16 Nov 2026 at 18:24:25, subject to the Cambridge Core terms of use, available at https://www.cambridge.org/core/terms. https://doi.org/10.1017/S0263574726103774

[4] O. Company, F. Marquet and F. Pierrot, "A new high-speed 4-DOF parallel robot synthesis and modeling issues," *IEEE Trans. Robot. Autom.* **19**(3), 411–420 (2003).

[5] S. Krut, O. Company, M. Benoit, H. Ota and F. Pierrot, "I4: A New Parallel Mechanism for SCARA Motions," **In:** *2003 International Conference on Robotics and Automation (ICRA)* (2003) pp. 1875–1880.

[6] V. Nabat, M. D. L. O. Rodriguez, O. Company, S. Krut and F. Pierrot, "Par4: Very hIgh Speed Parallel Robot for Pick-and-Place," **In:** *IEEE/RSJ International Conference on Intelligent Robots and Systems*, IEEE/RSJ (2005) pp. 1202–1207.

[7] S. Krut, O. Company, V. Nabat and F. Pierrot, " Heli4: A Parallel Robot for SCARA Motions with a Very Compact Traveling Plate and a Symmetrical Design," **In:** *2006 IEEE/RSJ International Conference on Intelligent Robots and Systems*, IEEE/RSJ (2006) pp. 1656–1661.

[8] T. Yang, A. Liu, H. Shen and L. Hang, " Topological Structure Synthesis of 3T1R Parallel Mechanism based on POC Equations," **In:** *9th International Conference on Intelligent Robotics and Applications*, ICIRA (2016) pp. 147–161.

[9] X. Kong and C. Gosselin, "Type synthesis of 3T1R 4-DOF parallel manipulators based on screw theory," *IEEE Trans. Robot. Autom.* **20**(2), 181–190 (2004).

[10] J. Angeles, "The qualitative synthesis of parallel manipulators," *ASME J. Mech. Des.* **126**(4), 617–674 (2004).

[11] L. Xu, Q. Chen, L. He and Q. Li, "Kinematic analysis and design of a novel 3T1R. 2-(PRR) 2RH hybrid manipulator," *Mech. Mach. Theory* **112**, 105–122 (2017).

[12] X. Zhang, W. Dong, L. Dai, J. Chen and X. Zhao, "2PPaRR-2PPaRU: Design, analysis, and optimization of a new 3TIR parallel manipulator with rotational pitch motion," *Proc. Inst. Mech. Eng. Pt. C J. Mech. Eng. Sci.* **236**(11), 6053–6063 (2022).

[13] X. Liu and J. Wang, "Some new parallel mechanisms containing the planar four-bar parallelogram," *Int. J. Robot. Res.* **22**(9), 717–732 (2003).

[14] O. Ma and J. Angeles, " Architecture Singularities of Platform Manipulators," **In:** *1991 IEEE International Conference on Robotics and Automation*, IEEE (1991) pp. 1542–1547.

[15] O. Ma and J. Angeles, " Optimum Architecture Design of Platform Manipulators," **In:** *5th IEEE International Conference on Advanced Robotics*, IEEE (1991) pp. 1130–1135.

[16] X. Yang, Z. Zhao, H. Xiong, Q. Li and Y. Lou, "Kinematic analysis and optimal design of a novel schönflies-motion parallel manipulator with rotational pitch motion for assembly operations," *ASME J. Mech. Rob.* **13**(4), 1–17 (2021).

[17] S. Kim, W. Kim and B. Yi, " Kinematic Analysis and Optimal Design of a 3T1R Type Parallel Mechanism," **In:** *IEEE International Conference on Robotics and Automation*, ICRA (2009) pp. 2199–2204.

[18] O. Salgado, O. Altuzarra, E. Amezua and A. Hernández, "A parallelogram-based parallel manipulator for Schönflies motion," *ASME J. Mech. Des.* **129**(12), 1243–1250 (2007).

[19] B. Yi, S. Kim, H. Kwak and W. Kim, "Multi-task oriented design of an asymmetric 3T1R type 4-DOF parallel mechanism," *Proc. IMechE, Part C: J. Mech. Eng. Sci.* **227**(10), 2236–2255 (2013).

[20] J. Angeles and C. López-Cajún, "Kinematic isotropy and the conditioning index of serial robotic manipulators," *Int. J. Rob. Res.* **11**, 560–571 (1992).

[21] R. Stoughton and T. Arai, "A modified Stewart platform manipulator with improved dexterity," *IEEE Trans. Rob. Autom.* **9**(2), 166–173 (1993).

[22] J. Wang, C. Wu and X. Liu, "Performance evaluation of parallel manipulators: Motion/force transmissibility and its index," *Mech. Mach. Theory* **45**(10), 1462–1476 (2010).

[23] X. Chen, F. Xie and X. Liu, "Evaluation of the maximum value of motion/force transmission power in parallel manipulators," *J. Mech. Eng.* **50**(3), 1–9 (2014).

[24] C. Gosselin and D. Zhang, "Stiffness analysis of parallel mechanisms using a lumped model," *Int. J. Robot. Res.* **17**(1), 17–27 (1998).

[25] A. Pashkevich, D. Chablat and P. Wenger, "Stiffness analysis of overconstrained parallel manipulators," *Mech and Mach Theory* **44**(5), 966–982 (2009).

[26] G. Wu, S. Bai and P. Hjørnet, "On the Stiffness of Three/four Degree-of-Freedom Parallel Pick-and-Place Robots with Four Identical Limbs," **In:** *2016 IEEE International Conference on Robotics and Automation*, ICRA (2016) pp. 861–866.

[27] H. Shen, Y. Tang, G. Wu, J. Li, T. Li and T. Yang, "Design and analysis of a class of two-limb non-parasitic 2T1R parallel mechanism with decoupled motion and symbolic forward position solution-influence of optimal arrangement of limbs onto the kinematics, dynamics and stiffness," *Mech. Mach. Theory* **172**, 104815 (2022).

[28] S. Yan, S. Ong and A. Nee, "Stiffness analysis of parallelogram-type parallel manipulators using a strain energy method," *Robot. Comput-Integr. Manuf.* **37**, 13–22 (2016).

[29] Z. Huang and Q. Li, "Type synthesis of symmetrical lower-mobility parallel mechanisms using the constraint-synthesis method," *Int J. Rob. Res.* **22**(1), 59–79 (2003).

[30] G. Dong, T. Sun, Y. Song, H. Gao and B. Lian, "Mobility analysis and kinematic synthesis of a novel 4-DoF parallel manipulator," *Robotica* **34**(5), 1010–1025 (2016).

[31] S. Zarkandi, "Kinematics of a star-triangle planar parallel manipulator," *J. Mech. Sci. Technol.* **25**(1), 3223–3230 (2011).

[32] J. Yuan and X. Zhang, "Kinematic Analysis of a Novel 4-DOFs Parallel Manipulator," *2006 IEEE International Conference on Information Acquisition*, ICIA (2006) pp. 534–539,

[33] C. Gosselin and J. Angeles, "Singularity analysis of closed-loop kinematic chains," *IEEE Trans. Robot. Autom.* **6**(3), 281–290 (1990).

Downloaded from https://www.cambridge.org/core. UNIVERSIDAD AUTONOMA METROPOLITANA, on 16 Nov 2026 at 18:24:25, subject to the Cambridge Core terms of use , available at https://www.cambridge.org/core/terms. https://doi.org/10.1017/S0263574726103774

[34] S. Balli and S. Chand, "Transmission angle in mechanisms," *Mech. Mach. Theory* **37**(2), 175–195 (2002).
[35] J. Dai and J. Jones, "A linear algebraic procedure in obtaining reciprocal screw systems," *J. Robotic Syst.* **20**, 401–412 (2003).
[36] F. Xie, X. Liu, L. Wang and J. Wang, "Optimal design and development of a decoupled A/B-axis tool head with parallel kinematics," *Adv. Mech. Eng.* **2**, 474602 (2010).
[37] M. Filipovic, "Relation between Euler–Bernoulli equation and contemporary knowledge in robotics," *Robotica* **30**(1), 1–13 (2012).
[38] X. Liu, I. Bonev, L. Wang and F. Xie, "Design of a three axis articulated tool head with parallel kinematics achieving desired motion/force transmission characteristics," *ASME J. Manuf. Sci. Eng.* **132**(2), 021009 (2010).
[39] X. Liu and J. Wang, "A new methodology for optimal kinematic design of parallel mechanisms," *Mech. Mach. Theory* **42**(9), 1210–1224 (2007).

Appendix A. The expressions of the transmission wrench screw

$l_{11} = l_1 \cos\theta_{11}\,(z - d_1 - l_1 \sin\theta_{11})\,, m_1 = -l_1 \sin\theta_{11}\,(b_2 - a_1 - y)\,, n_1 = l_1 \sin\theta_{11}\,(z - d_1 - l_1 \sin\theta_{11})$

$p_1 = l_1 \sin\theta_{11}\,((d_1 + l_1 \sin\theta_{11})\,(b_2 - y) - za_1)\,, q_1 = -\,(d_1 + l_1 \sin\theta_{11} - z)\,(-xl_1 \sin\theta_{11} + zl_1 \cos\theta_{11})\,, r_1 = 0$

$l_{21} = -l_1 \sin\theta_{21}\,(x - b_1 \cos\phi + a_2)\,, m_2 = l_1 \cos\theta_{21}\,(d_2 + l_1 \sin\theta_{21} - z - b_1 \sin\phi)\,, p_2 = 0,$

$l_{31} = l_1 \cos\theta_{31}\,(z - d_3 - l_1 \sin\theta_{31})\,, n_2 = l_1 \sin\theta_{21}\,(d_2 + l_1 \sin\theta_{21} - z - b_1 \sin\phi)\,, r_2 = 0,$

$q_2 = -l_1 \sin\theta_{21}\,((d_2 + l_1 \sin\theta_{21})\,(x - b_1 \cos\phi) + a_2\,(z + b_1 \sin\phi))\,, m_3 = -l_1 \sin\theta_{31}\,(a_1 - y - b_2)\,,$

$n_3 = l_1 \sin\theta_{31}\,(z - d_3 - l_1 \sin\theta_{31})\,, p_3 = l_1 \sin\theta_{31}\,((d_3 + l_1 \sin\theta_{31})\,(-y - b_2) + za_1)\,,$

$q_3 = -\,(d_3 + l_1 \sin\theta_{31} - z)\,(-xl_1 \sin\theta_{31} + zl_1 \cos\theta_{31})\,, m_4 = l_1 \cos\theta_{41}\,(d_4 + l_1 \sin\theta_{41} - z)\,,$

$n_4 = l_1 \sin\theta_{41}\,(d_4 + l_1 \sin\theta_{41} - z)\,, r_3 = 0, l_{41} = -l_1 \sin\theta_{41}\,(x - a_2)\,, p_4 = 0,$

$q_4 = l_1 \sin\theta_{41}\,(za_2 - xd_4 - xl_1 \sin\theta_{41})\,, r_4 = 0.$

Appendix B. The expressions of the Jacobian matrix

The Jacobian matrix of the PPaRU limb is:

$$\$^i_{Pa1} = \begin{bmatrix} \boldsymbol{u}_{a_ib_i} \\ (\boldsymbol{r}_{Bi} - \boldsymbol{o}') \times \boldsymbol{u}_{a_ib_i} \end{bmatrix}, \$^i_{Pa2} = \begin{bmatrix} -\boldsymbol{y} \\ -(\boldsymbol{r}_{Bi} - \boldsymbol{o}') \times \boldsymbol{y} \end{bmatrix}, \$^i_{Pa3} = \begin{bmatrix} -\boldsymbol{u}_{a_ib_i} \times \boldsymbol{y} \\ -(\boldsymbol{r}_{Bi} - \boldsymbol{o}') \times (\boldsymbol{u}_{a_ib_i} \times \boldsymbol{y}) \end{bmatrix}, \$^i_{Pa4} = \begin{bmatrix} \boldsymbol{0} \\ \boldsymbol{u}_{a_ib_i} \end{bmatrix},$$

$$\$^i_{Pa5} = \begin{bmatrix} \boldsymbol{0} \\ -\boldsymbol{y} \end{bmatrix}, \$^i_{Rod1} = \begin{bmatrix} \boldsymbol{u}_{b_ic_i} \\ (\boldsymbol{r}_{Ci} - \boldsymbol{o}') \times \boldsymbol{u}_{b_ic_i} \end{bmatrix}, \$^i_{Rod2} = \begin{bmatrix} \boldsymbol{x} \times \boldsymbol{u}_{b_ic_i} \\ (\boldsymbol{r}_{Ci} - \boldsymbol{o}') \times (\boldsymbol{x} \times \boldsymbol{u}_{b_ic_i}) \end{bmatrix}, \$^i_{Rod3} = \begin{bmatrix} \boldsymbol{x} \\ (\boldsymbol{r}_{Ci} - \boldsymbol{o}') \times \boldsymbol{x} \end{bmatrix},$$

$$\$^i_{Rod4} = \begin{bmatrix} \boldsymbol{0} \\ \boldsymbol{u}_{b_ic_i} \end{bmatrix}, \$^i_{Rod5} = \begin{bmatrix} \boldsymbol{0} \\ \boldsymbol{x} \times \boldsymbol{u}_{b_ic_i} \end{bmatrix}, \$^i_{Rod6} = \begin{bmatrix} \boldsymbol{0} \\ \boldsymbol{x} \end{bmatrix}, \$^i_{Rod7} = \begin{bmatrix} \boldsymbol{y} \\ (\boldsymbol{r}_{Ci} - \boldsymbol{o}') \times \boldsymbol{y} \end{bmatrix}, \$^i_{Rod8} = \begin{bmatrix} \boldsymbol{z} \\ (\boldsymbol{r}_{Ci} - \boldsymbol{o}') \times \boldsymbol{z} \end{bmatrix},$$

$$\$^i_{Rod9} = \begin{bmatrix} \boldsymbol{x} \\ (\boldsymbol{r}_{Ci} - \boldsymbol{o}') \times \boldsymbol{x} \end{bmatrix}, \$^i_{Rod10} = \begin{bmatrix} \boldsymbol{0} \\ \boldsymbol{y} \end{bmatrix}, \$^i_{Rod11} = \begin{bmatrix} \boldsymbol{0} \\ \boldsymbol{z} \end{bmatrix}, \$^i_{Rod12} = \begin{bmatrix} \boldsymbol{0} \\ \boldsymbol{x} \end{bmatrix}, \$^i_{q1} = \begin{bmatrix} \boldsymbol{0} \\ -\boldsymbol{u}_{a_ib_i} \times \boldsymbol{y} \end{bmatrix},$$

$$\$^i_{q2} = \begin{bmatrix} \boldsymbol{x} \\ (\boldsymbol{r}_{Bi} - \boldsymbol{o}') \times \boldsymbol{x} \end{bmatrix}, \$^i_{q3} = \begin{bmatrix} \boldsymbol{x} \\ (\boldsymbol{r}_{Ci} - \boldsymbol{o}') \times \boldsymbol{x} \end{bmatrix}, \$^i_{q4} = \begin{bmatrix} \boldsymbol{y} \\ (\boldsymbol{r}_{Ci} - \boldsymbol{o}') \times \boldsymbol{y} \end{bmatrix}, \$_{ac} = \begin{bmatrix} \boldsymbol{0} \\ \boldsymbol{z} \end{bmatrix}$$

where $\boldsymbol{u}_{a_ib_i}$ and $\boldsymbol{u}_{b_ic_i}$ denote the unit vectors of links A_iB_i and B_iC_i, respectively, and $\boldsymbol{r}_{Bi}, \boldsymbol{r}_{Ci}$ and $\boldsymbol{o}'$ denote the positions of points $B_i, C_i (i = 1, 3)$ and o' in the fixed frame.

The Jacobian matrix of the PPaRR limb is:

$$\$^i_{Pa1} = \begin{bmatrix} \boldsymbol{u}_{a_ib_i} \\ (\boldsymbol{r}_{Bi} - \boldsymbol{o}') \times \boldsymbol{u}_{a_ib_i} \end{bmatrix}, \$^i_{Pa2} = \begin{bmatrix} \boldsymbol{x} \\ (\boldsymbol{r}_{Bi} - \boldsymbol{o}') \times \boldsymbol{x} \end{bmatrix}, \$^i_{Pa3} = \begin{bmatrix} \boldsymbol{u}_{a_ib_i} \times \boldsymbol{x} \\ (\boldsymbol{r}_{Bi} - \boldsymbol{o}') \times (\boldsymbol{u}_{a_ib_i} \times \boldsymbol{x}) \end{bmatrix}, \$_{ac} = \begin{bmatrix} \boldsymbol{0} \\ \boldsymbol{z} \end{bmatrix}$$

Downloaded from https://www.cambridge.org/core. UNIVERSIDAD AUTONOMA METROPOLITANA, on 16 Nov 2026 at 18:24:25, subject to the Cambridge Core terms of use, available at https://www.cambridge.org/core/terms. https://doi.org/10.1017/S0263574726103774

$$\$^i_{Pa4}=\begin{bmatrix}\mathbf{0}\\ \boldsymbol{u}_{a_ib_i}\end{bmatrix},\$^i_{Pa5}=\begin{bmatrix}\mathbf{0}\\ \boldsymbol{x}\end{bmatrix},\$^i_{Rod1}=\begin{bmatrix}\boldsymbol{u}_{b_ic_i}\\ (\boldsymbol{r}_{Ci}-\boldsymbol{o}')\times\boldsymbol{u}_{b_ic_i}\end{bmatrix},\$^i_{Rod2}=\begin{bmatrix}\boldsymbol{y}\times\boldsymbol{u}_{b_ic_i}\\ (\boldsymbol{r}_{Ci}-\boldsymbol{o}')\times\left(\boldsymbol{y}\times\boldsymbol{u}_{b_ic_i}\right)\end{bmatrix},$$

$$\$^i_{Rod3}=\begin{bmatrix}\boldsymbol{y}\\ (\boldsymbol{r}_{Ci}-\boldsymbol{o}')\times\boldsymbol{y}\end{bmatrix},$$

$$\$^i_{Rod4}=\begin{bmatrix}\mathbf{0}\\ \boldsymbol{u}_{b_ic_i}\end{bmatrix},\$^i_{Rod5}=\begin{bmatrix}\mathbf{0}\\ \boldsymbol{y}\times\boldsymbol{u}_{b_ic_i}\end{bmatrix},\$^i_{Rod6}=\begin{bmatrix}\mathbf{0}\\ \boldsymbol{y}\end{bmatrix},\$^i_{q1}=\begin{bmatrix}\mathbf{0}\\ \boldsymbol{u}_{a_ib_i}\times\boldsymbol{x}\end{bmatrix},\$^i_{q2}=\begin{bmatrix}\boldsymbol{y}\\ (\boldsymbol{r}_{Bi}-\boldsymbol{o}')\times\boldsymbol{y}\end{bmatrix},$$

$$\$^i_{q3}=\begin{bmatrix}\boldsymbol{y}\\ (\boldsymbol{r}_{Ci}-\boldsymbol{o}')\times\boldsymbol{y}\end{bmatrix}.$$

where $\boldsymbol{u}_{a_ib_i}$ and $\boldsymbol{u}_{b_ic_i}$ denote the unit vectors of links A_iB_i and B_iC_i, respectively, and $\boldsymbol{r}_{Bi}, \boldsymbol{r}_{Ci}$ and $\boldsymbol{o}'$ denote the positions of points B_i, $C_i(i=2,4)$ and o' in fixed frame.

Cite this article: X. Zhang, A. Ji, S. Wen, A. Jiang, Y. Sun, Z. Yang and Q. Qi (2026). "Performance analysis and optimization of a modified Schoenflies motion parallel manipulator with decoupled pitch motion", Robotica **44**, 1743–1765. https://doi.org/10.1017/S0263574726103774

Downloaded from https://www.cambridge.org/core. UNIVERSIDAD AUTONOMA METROPOLITANA, on 16 Nov 2026 at 18:24:25, subject to the Cambridge Core terms of use, available at https://www.cambridge.org/core/terms. https://doi.org/10.1017/S0263574726103774